

Utah State University

DigitalCommons@USU

All Graduate Theses and Dissertations

Graduate Studies

5-2011

A Fully Automatic Segmentation Method for Breast Ultrasound Images

Juan Shan
Utah State University

Follow this and additional works at: <https://digitalcommons.usu.edu/etd>



Part of the [Computer Sciences Commons](#)

Recommended Citation

Shan, Juan, "A Fully Automatic Segmentation Method for Breast Ultrasound Images" (2011). *All Graduate Theses and Dissertations*. 905.

<https://digitalcommons.usu.edu/etd/905>

This Dissertation is brought to you for free and open access by the Graduate Studies at DigitalCommons@USU. It has been accepted for inclusion in All Graduate Theses and Dissertations by an authorized administrator of DigitalCommons@USU. For more information, please contact digitalcommons@usu.edu.



A FULLY AUTOMATIC SEGMENTATION METHOD FOR
BREAST ULTRASOUND IMAGES

by

Juan Shan

A dissertation submitted in partial fulfillment
of the requirements for the degree

of

DOCTOR OF PHILOSOPHY

in

Computer Science

Approved:

Dr. Heng-Da Cheng
Major Professor

Dr. Daniel W. Watson
Committee Member

Dr. Stephen J. Allan
Committee Member

Dr. Renée Bryce
Committee Member

Dr. YangQuan Chen
Committee Member

Dr. Byron R. Burnham
Dean of Graduate Studies

UTAH STATE UNIVERSITY
Logan, Utah

2011

Copyright © Juan Shan 2011

All Rights Reserved

ABSTRACT

A Fully Automatic Segmentation Method for
Breast Ultrasound Images

by

Juan Shan, Doctor of Philosophy

Utah State University, 2011

Major Professor: Dr. Heng-Da Cheng
Department: Computer Science

Breast cancer is the second leading cause of death of women worldwide. Accurate lesion boundary detection is important for breast cancer diagnosis. Since many crucial features for discriminating benign and malignant lesions are based on the contour, shape, and texture of the lesion, an accurate segmentation method is essential for a successful diagnosis. Ultrasound is an effective screening tool and primarily useful for differentiating benign and malignant lesions. However, due to inherent speckle noise and low contrast of breast ultrasound imaging, automatic lesion segmentation is still a challenging task.

This research focuses on developing a novel, effective, and fully automatic lesion segmentation method for breast ultrasound images. By incorporating empirical domain knowledge of breast structure, a region of interest is generated. Then, a novel enhancement algorithm (using a novel phase feature) and a newly developed neutrosophic clustering method are developed to detect the precise lesion boundary.

Neutrosophy is a recently introduced branch of philosophy that deals with paradoxes, contradictions, antitheses, and antinomies. When neutrosophy is used to segment images with vague boundaries, its unique ability to deal with uncertainty is brought to bear. In this work, we apply neutrosophy to breast ultrasound image segmentation and propose a new clustering method named neutrosophic *l*-means. We compare the proposed method with traditional fuzzy c-means clustering and three other well-developed segmentation methods for breast ultrasound images, using the same database. Both accuracy and time complexity are analyzed. The proposed method achieves the best accuracy (TP rate is 94.36%, FP rate is 8.08%, and similarity rate is 87.39%) with a fairly rapid processing speed (about 20 seconds). Sensitivity analysis shows the robustness of the proposed method as well. Cases with multiple-lesions and severe shadowing effect (shadow areas having similar intensity values of the lesion and tightly connected with the lesion) are not included in this study.

(110 pages)

*This work is dedicated to my grandma Jingzhen Dai,
my parents, Lianjia Shan and Yanhua Su,
my husband, Yuxuan Wang,
and my son, Kevin Wang.*

ACKNOWLEDGMENTS

First of all, I would like to express my sincere appreciation and gratitude to my advisor, Dr. Heng-Da Cheng. Without his consistent and patient academic guidance, I would never have been able to finish this dissertation. His encouragement and career guidance have also been very important for me. His direction in my academic pursuits has opened many doors for me. I am very grateful to my committee members, Dr. Yangquan Chen, Dr. Dan Watson, Dr. Steve Allan, and Dr. Renée Bryce, for their comments, advice, and contributions to this research.

I wish to thank my colleagues and friends who assisted me during my study at Utah State University. Special thanks to my colleagues, the group members of the CVPRIP, Wen Ju, Yanhui Guo, Ming Zhang and Chenguang Liu, for their help and cooperation.

Particularly, I would like to thank my husband, Yuxuan Wang, who is also a member in the CVPRIP group, for his suggestions, moral support, and warm encouragement at all the times. My sincere appreciation goes to my parents and my parents-in-law, who helped me by taking care of my 2-year-old son, Kevin Wang. Their help enabled me to focus on my dissertation research. Thanks to my dear little son, Kevin; he is the most beloved person in my life and also my endless source of power and encouragement.

Special thanks to the support of the Second Affiliated Hospital of Harbin Medical University (Harbin, China). The provided image database and doctors' participation and collaboration in the research were very important for me to complete this work.

Juan Shan

CONTENTS

	Page
ABSTRACT	iii
ACKNOWLEDGMENTS	vi
LIST OF TABLES	ix
LIST OF FIGURES	x
CHAPTER	
1 INTRODUCTION	1
1.1 Ultrasound Imaging	1
1.2 Computer-Aided Diagnosis	2
1.3 Lesion Segmentation	4
1.3.1 Histogram Thresholding and Region Growing	5
1.3.2 Model-Based Methods	6
1.3.3 Machine Learning Methods	8
1.3.4 Watershed Methods	9
1.4 The Proposed Method	11
2 AUTOMATIC REGION OF INTEREST GENERATION	14
2.1 Automatic Seed Point Selection	15
2.1.1 The Proposed Seed Point Selection Algorithm	16
2.1.2 Experiment Results of the Seed Point Selection Algorithm	23
2.2 Region Growing	26
3 SPECKLE REDUCTION	30
4 IMAGE ENHANCEMENT USING LOCAL PHASE INFORMATION	35
4.1 Local Phase 1-D Detection	36
4.2 From 1-D Signal to 2-D Image	44
5 LESION DETECTION BY NEUTROSOPHIC L-MEANS	54

5.1 Fuzzy C-Means	54
5.2 Neutrosophy	55
5.3 Definitions of Neutrosophic Components for BUS Image Segmentation	58
5.4 Neutrosophic L-Means.....	61
6 EXPERIMENT RESULTS.....	64
6.1 Database.....	64
6.2 Evaluation Metrics	65
6.2.1 Area Error Metrics	65
6.2.2 Boundary Error Metrics	66
6.3 Comparison of NLM and Fuzzy C-Means.....	67
6.4 Comparison of the Proposed Method with Other BUS Segmentation Methods ...	73
6.5 Sensitivity Analysis	78
6.5.1 Effect of Tuning Membership Parameter m	79
6.5.2 Effect of Tuning Window Size w	79
6.5.3 Effect of Tuning Threshold λ	80
6.6 Limitations of the Proposed Method.....	81
7 CONCLUSIONS AND FUTURE DIRECTIONS FOR RESEARCH.....	83
REFERENCES	85
CURRICULUM VITAE.....	95

LIST OF TABLES

Table	Page
1.1 Summary of Segmentation Methods for BUS Images.....	10
2.1 Comparison of the Proposed Seed Point Selection Algorithm and the Active Contour Method [21]	26
3.1 Comparison of De-speckle Effect and Time Complexity of the Method in [58] and SRAD [50]	34
6.1 Comparison of NLM and FCM.....	72
6.2 Comparison of Accuracy of the Active Contour Method [21], Level-Set Method [28], Watershed Method [70], and the Proposed Method.....	78
6.3 Comparison of Time Complexity of the Active Contour Method [21], Level Set Method [28], Watershed Method [70], and the Proposed Method	78
6.4 Performance and Standard Deviation for Different Values of m	79
6.5 Performance and Standard Deviation for Different Values of w	80
6.6 Performance and Standard Deviation for Different Values of λ	80

LIST OF FIGURES

Figure	Page
1.1 A CAD system for breast cancer diagnosis.....	3
1.2 Flowchart of the proposed method.....	12
2.1 (a) Original image. (b) Result after speckle reduction using SRAD [50].	17
2.2 (a) Result after iterative threshold selection. (b) Result after deleting boundary-connected region	20
2.3 (a) The winning region. (b) Selected seed point	22
2.4 Results of two cases: (a) and (c) are the results of the proposed seed point selection algorithm; (b) and (d) are the results of the seed point selection algorithm in [21]	25
2.5 (a) Original image with seed point marked. (b) Result of region growing. (c) ROI.....	28
3.1 (a) The ROI cut from the original image. (b) Result of SRAD [50] after five iterations. (c) Result of the method described in [58].....	32
4.1 Fourier series of (a) a step edge, (b) an intensity ridge. Dashed lines are the first four Fourier components and solid lines are the sum of these components [62].....	35
4.2 (a) A 1-D signal with step edges (1, 2) and intensity ridge (3). (b) Local phase scalogram obtained by a bank of Log-Gabor filters. (c) Local phase accumulation by adding up the above local phase scalogram and divided by the total number of scales.....	39
4.3 Local phase profiles at different scales	41
4.4 (a) A 1-D signal with step edges (1, 2) and intensity ridge (3). (b) Local phase scalogram obtained by a bank of Log-Gabor filters (max wavelength = 36.0). (c) Local phase accumulation by adding up the above local phase scalogram and divided by the total number of scales.....	42
4.5 Local phase strengthening function (Eq. (14)).....	43

4.6	Local phase accumulation before and after the strengthening function (Eq. (14)).....	45
4.7	(a) The original image. (b) Phase summation feature image obtained by Eq. (19). (c) PMO feature image obtained by Eq. (20).....	49
4.8	(a) ROI. (b) De-speckled image by the method described [58]. (c) PMO feature image. (d) PMO feature image after multiplying with the de-speckled image in (b). (e) PMO feature image after median filtering. (f) Enhanced PMO image after applying Eqs. (22) and (23).....	51
5.1	Relationships among neutrosophic set and other sets	58
5.2	True foreground (a) and false foregrounds (b, c and d)	63
6.1	Areas corresponding to TP, FP, and FN regions.....	67
6.2	(a) Automatic ROI generation from original image. (b) Enhanced PMO image. (c) Output of FCM. (d) Output of NLM. (e) Manually delineation by radiologist.....	68
6.3	(a) Automatic ROI generation from original image. (b) Enhanced PMO image. (c) Output of FCM. (d) Output of NLM. (e) Manually delineation by radiologist.....	70
6.4	(a) The original image. (b) Manual delineation by radiologist. (c) Output of the method in [21]. (d) Output of the method in [28]. (d) Output of the method in [70]. (e) Output of the proposed method.....	76
6.5	(a) A case with posterior shadowing. (b) Manual delineation by radiologist. (c) Output of the proposed method.....	81
6.6	(a) A case with multiple lesions. (b) Manual delineation by radiologist. (c) Output of the proposed method.....	82

CHAPTER 1

INTRODUCTION

Breast cancer is the second leading cause of death for women worldwide, and more than 8% of all women will suffer this disease during their lifetime [1]. According to cancer statistics 2010, it is estimated that 209,060 new cases of breast cancer will be diagnosed and approximately 40,230 deaths are expected in the United States alone [2]. Since the causes of breast cancer still remain unknown, early detection is the key to reduce the death rate (40% or more) [3]. The earlier the cancers are detected, the better the treatment that can be provided. Early detection requires an accurate and reliable diagnosis which should also be able to distinguish between benign and malignant tumors. Further, a good detection approach should produce both a low false positive rate and a false negative rate.

1.1 Ultrasound Imaging

Until recently, the most effective modality for detecting and diagnosing has been mammography [3, 4]. However, there are limitations of mammography in breast cancer detection. Many unnecessary (65–85%) biopsy operations are due to the low specificity of mammography [5]. The unnecessary biopsies not only increase the cost, but also make the patients suffer from emotional pressure. Mammography has also proven less effective in detecting breast cancer in adolescent women with dense breasts. In addition, the ionizing radiation of mammography might be harmful for both patients and radiologists.

Ultrasound (US) imaging is an important alternative to mammography. Researchers and practitioners are showing an increasing interest in the use of ultrasound images for breast cancer detection [6-8]. Statistics show that more than one out of every four study

on breast cancer detection is based on ultrasound images, and the proportion is rapidly increasing [9]. Studies have demonstrated that using US images can discriminate benign and malignant masses with a high accuracy [10, 11]. Use of ultrasound can increase over all cancer detection by 17% [12] and reduce the number of unnecessary biopsies by 40% which can save as much as \$1 billion per year in the United States alone [13]. Breast ultrasound (BUS) imaging is superior to mammography in the following ways. (1) Since it requires no radiation, ultrasound examination is more convenient and safer than mammography for patients and radiologists in daily clinical practice [14]. It is also cheaper and faster than mammography. Thus, ultrasound is especially suitable for the low-resource countries in different continents [15]. (2) Ultrasound techniques are more sensitive than mammography for detecting abnormalities in dense breasts; hence, it is more valuable for women younger than 35 years of age [12]. (3) There is a high rate of false positives in mammography which causes a lot of unnecessary biopsies [11]. In contrast, the accuracy rate of BUS imaging in the diagnosis of simple cysts is much higher [10]. Thus, US imaging has become one of the most important diagnostic tools for breast cancer detection.

1.2 Computer-Aided Diagnosis

Since sonography is much more operator-dependent than mammography, reading ultrasound image requires well-trained and experienced radiologists. Further, even well-trained experts may have a high inter-observer variation rate; therefore, computer-aided diagnosis (CAD) is has been investigated to help radiologists in making accurate diagnoses. One advantage of a CAD system is that it can obtain some features, such as

computational features and statistical features, which cannot be obtained visually and intuitively by medical doctors. Another advantage is that CAD can minimize the operator-dependent nature inherent in ultrasound imaging [16] and make the diagnosis process reproducible. It should be noted that research into the use of CAD is not done so with an eye toward eliminating doctors or radiologists, rather the goal is to provide doctors and radiologists a second opinion and help them to increase the diagnosis accuracy, reduce biopsy rate, and save them time and effort.

Generally, ultrasound CAD systems for breast cancer detection involve four stages, as shown in Figure 1.1.

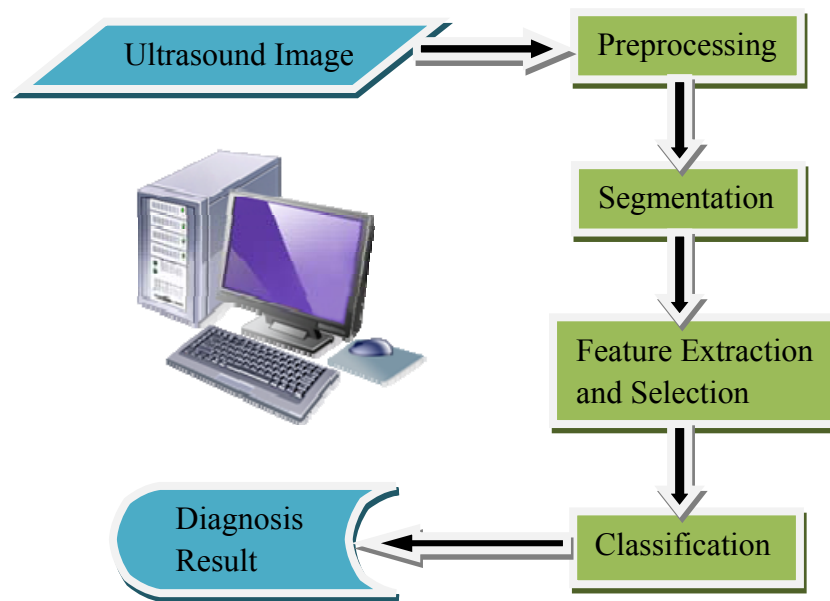


Figure 1.1. A CAD system for breast cancer diagnosis.

1. Image preprocessing: The task of image preprocessing is to enhance the image and to reduce speckle without destroying the important features of BUS images for diagnosis.
2. Image segmentation: Image segmentation divides the image into non-overlapping regions, and it separates the objects (lesions) from the background. The boundaries of the lesions are delineated for feature extraction.
3. Feature extraction and selection: This step is to find a feature set of breast cancer lesions that can accurately distinguish lesion/non-lesion or benign/malignant. The feature space could be very large and complex, so extracting and selecting the most effective features is very important.
4. Classification: Based on the selected features, the suspicious regions will be classified into different categories, such as benign findings and malignancy. Many machine learning techniques such as linear discriminant analysis (LDA), support vector machine (SVM) and artificial neural network (ANN) have been studied for lesion classification.

1.3 Lesion Segmentation

Segmentation is an important step of CAD systems. Both automation and accuracy of segmentation is crucial. Automation of segmentation is important because it facilitates the complete automation of the CAD system. A fully automatic CAD can minimize the effect of the operator-dependent nature inherent in ultrasound imaging [16] and make the diagnosis process reproducible. Accuracy of segmentation is important because many crucial features for discriminating benign and malignant lesions are based on the contour,

shape and texture of the lesion (ACR BI-RADS lexicon [17]). These features can be effectively extracted after the lesion boundary is correctly detected. Thus, an accurate segmentation method is essential for a correct diagnosis. However, there are characteristic artifacts, such as attenuation, speckle, shadows, and signal dropout, which make the segmentation task complicated; these artifacts are due to the orientation dependence of acquisition that can result in missing boundaries. Further complications arise as the contrast between areas of interest is often low [18]. How to do one of the oldest image processing tasks, image segmentation, for breast ultrasound, is a challenging task.

Many techniques have been developed for BUS segmentation. They are categorized into histogram thresholding, region growing, model-based (active contour, level set, Markov random field), machine learning, and watershed methods.

1.3.1 Histogram Thresholding and Region Growing

Simple histogram thresholding [19, 20] or region-growing algorithms [21, 22] can find the preliminary lesion boundary. In a histogram thresholding method, an intensity threshold is chosen at the valley of the image histogram to separate the image into background and foreground. For a region growing method, a region is grown from the seed point (start point) by adding similar neighboring pixels. Although efficient, these methods cannot generate a precise boundary because their over-simplified concepts and the high sensitivity to noise. However, they can serve as an intermediate step to provide a rough contour [21] or can be combined with post-processing procedures such as morphological operations [19, 20, 23], disk expansion [24], Bayesian neural network [12],

function optimization [25, 26], etc. For example, in the thresholding algorithm [19, 20], firstly, the regions of interest (ROIs) were preprocessed with a 4×4 median filter to reduce the speckle noise and to enhance the features. Second, a 3×3 unsharp filter was constructed using the negative of a two-dimensional Laplacian filter to emphasize the elements with meaningful signal level and to enhance the contrast between object and background. Third, the ROIs were converted to a binary image by thresholding. The threshold was determined by the histogram of ROIs. If a valley of a histogram between 33% and 66% of the pixel population could be found, this intensity value was selected as the threshold. If there was no such valley in that range, the intensity of 50% of the pixel population was selected as the threshold value. Finally, the selected nodule's boundary pixels were obtained using morphologic operations.

1.3.2 Model-Based Methods

Model-based methods have strong noise-resistant abilities and are relatively stable at sonography demarcation. Commonly used models include level set [27-29], active contours [21, 30-33], Markov random fields (MRF) [34-38], etc.

For instance, Sarti et al. [29] discussed a level set maximum likelihood method to achieve a maximum likelihood segmentation of the target. The Rayleigh probability distribution was utilized to model gray level behavior of ultrasound images. A partial differential equation-based flow was derived as the steepest descent of an energy function taking into account the density probability distribution of the gray levels, as well as smoothness constraints. A level set formulation for the associated flow was derived to

search the minimal value of the model. Finally, the image was segmented according to the minimum energy.

Madabhushi and Metaxas [21] combined intensity, texture information, and empirical domain knowledge used by radiologists with an active contour model in an attempt to limit the effects of shadowing and false positives. Their method requires training but in the small database. Using manual delineation of the mass by a radiologist as a reference, and the Hausdorff distance and average distance as boundary error metrics, they showed that their method is independent of the number of training samples, shows good reproducibility with respect to parameters, and gives a true positive area of 74.7%. Some active contour models have been applied to 3-D ultrasound segmentation, such as [30-33].

Boukerroui et al. [34] used a Markov random field to model the region process and to focus on the adaptive characteristics of the algorithm. Their method introduced a function to control the adaptive properties of the segmentation process, and took into account both local and global statistics during the segmentation process. A new formulation of the segmentation problem was utilized to control the effective contribution of each statistical component. The merit of MRF modeling is that it provides a strong exploitation of the pixel correlations. The segmentation results can be further enhanced via the application of maximum a posteriori segmentation estimation scheme based on the Bayesian learning paradigm [18].

In most model-based approaches, an energy function is formulated, and the segmentation problem is transformed as finding the minimum (or maximum) of the energy function iteratively. However, the iterations on calculating energy functions and

reformulating the models are always time-consuming, especially for complex BUS images; and many models are semi-automatic with the requirement of pre-labeled ROI or manually initialized contour.

1.3.3 Machine Learning Methods

Machine learning methods (such as neural network and support vector machine) [39-43] are popular in image segmentation, which transform the segmentation problem into a classification decision based on a set of input features. In [42], Dokur and Ölmez proposed a neural network based segmentation method. Images were divided into square blocks, and features were extracted from each block using the discrete cosine transform (DCT). Then a three-layer hybrid neural network was trained to classify the blocks into two categories: background and foreground. The method was applied on the region of interest (ROI) which needed to be selected by the user. Kotropoulos and Pitas [39] employed a support vector machine with a radial basis function kernel to classify different patterns. In this method, patterns were collected by a running window with size of 15x15 over the entire image. To train the SVM, 1128 positive patterns (lesion) and 1128 negative patterns (background) were selected from the training set. Experiments showed that the trained SVM could generate reasonable segmentation result.

For machine learning methods, feature selection and training process are two key steps that play an important role on segmentation result. If features are sufficiently distinguishable and the method is well trained, machine learning methods can generate satisfactory lesion contours. However, over-training or insufficient training (trapped by

local minimum) may severely affect the segmentation performance on new data. And the training process is usually quite time-consuming.

1.3.4 Watershed-Based Methods

Watershed-based approaches have shown promising performances for ultrasound image segmentation. The methods consider image as topographic surface wherein the grey level of a pixel is interpreted as its altitude. Water flows along a path to finally reach a local minimum. The biggest challenge for such methods is over-segmentation; to address the problem, many approaches have been proposed and can be categorized into two types: marker-controlled [44-46] and cell competition [47-49].

Marker-controlled methods inundate the gradient landscape of image and define watersheds when the flooding of distinct markers rendezvous with each other. Hence, the identification of makers is very crucial in solving the over-segmentation problem. The method proposed in [44] was a texture-based approach that selected the marker candidates as seeds for the water-level immersion. A self-organization map was trained to identify the texture of lesions as the flooding markers. Distinctively, the method in [45] adopted a thresholding and morphological operation scheme to seek flooding markers. It required a heuristic estimation of the best thresholding of markers to achieve the task of lesion delineation.

Cell competition approaches, on the other hand, alleviate the over-segmentation problem in a different way. A two-pass watershed transformation [47] was performed to generate the cell tessellation on the original ultrasound image or ROI. In this method, a competition scheme based on the cell tessellation was carried out by allowing merge and

split operations of cells. The cost function was devised to characterize boundary saliency and regional homogeneity of an image partition, and it drove the competition process to converge to a prominent component structure. However, neither marker-controlled nor cell competition approaches guarantee to solve the over-segmentation problem completely [48].

Commonly used segmentation approaches are summarized in Table 1.1.

Table 1.1. Summary of Segmentation Methods for BUS Images.

Methods	Descriptions	Advantages	Disadvantages
Histogram thresholding	Threshold value is selected to segment the image.	Simple and fast.	Only works for bimodal histograms and has no good results for BUS images
Region growing	Region is grown from the seed point by adding similar neighboring pixels.	The concept is simple. Multiple stop criteria can be chosen.	Seed point is required; sensitive to noise.
Model-based (includes active contour, level set, Markov random fields)	A model is used to formulate the lesion contour, and the model is revised based on local features such as edges, intensity gradient, texture, and so on.	Robust, self-adapting in search of a minimal energy state.	Time-consuming; pre-labeled ROI or initial contour is required; easy to get stuck in local minima states.
Machine learning	Features to separate the lesion from the background are extracted first, and a machine learning method is trained to do the classification based on pixel-level or region-level.	Stable; different lesion characteristics can be incorporated by feature extraction.	Long training time; over-training problem; test images should come from the same platform as the training images.
Watershed (includes marker-controlled watershed and cell-competition watershed)	Considers image as topographic surface wherein grey level of a pixel is interpreted as its altitude. Water flows along a path to finally reach a local minimum.	It ensures closed region boundaries.	Over-segmentation problem is not completely solved.

In summary, the major drawbacks of current methods are: 1) human interactions such as the pre-labeled ROIs or manually initialized contours are required, which impede full automation; 2) intensity features are most typically used for boundary detection. Since BUS images have low contrast and are degraded by speckle noise, features based on intensity gradients are always sensitive to noise and cannot guarantee accurate segmentation result; 3) reformulating the models and training the methods are always time-consuming, especially for complex BUS images. As the image resolution increases, the computational complexity for processing a BUS image also increases.

1.4 The Proposed Method

In this research, a novel lesion segmentation method is proposed to overcome the above problems. Figure 1.2 shows the flowchart of the proposed method. The method is composed of four major steps: ROI generation, speckle reduction, image enhancement and neutrosophic l-means clustering. With the exception of the speckle reduction method [50], the algorithms in this work are newly proposed. The novelties and contributions of this work are:

1. The method achieves complete automation and accurate segmentation at the same time. For medical image segmentation, high accuracy requires more human intervention, and realizing complete automation is often at the expense of accuracy. The proposed method successfully resolves such dilemmas.
2. An automatic ROI generation method is developed. The ROI is a relatively small rectangular region taken from the original image. Further operations are

conducted only on the ROI. Cutting off the complicated background not only speeds up the segmentation process, but also increases accuracy.

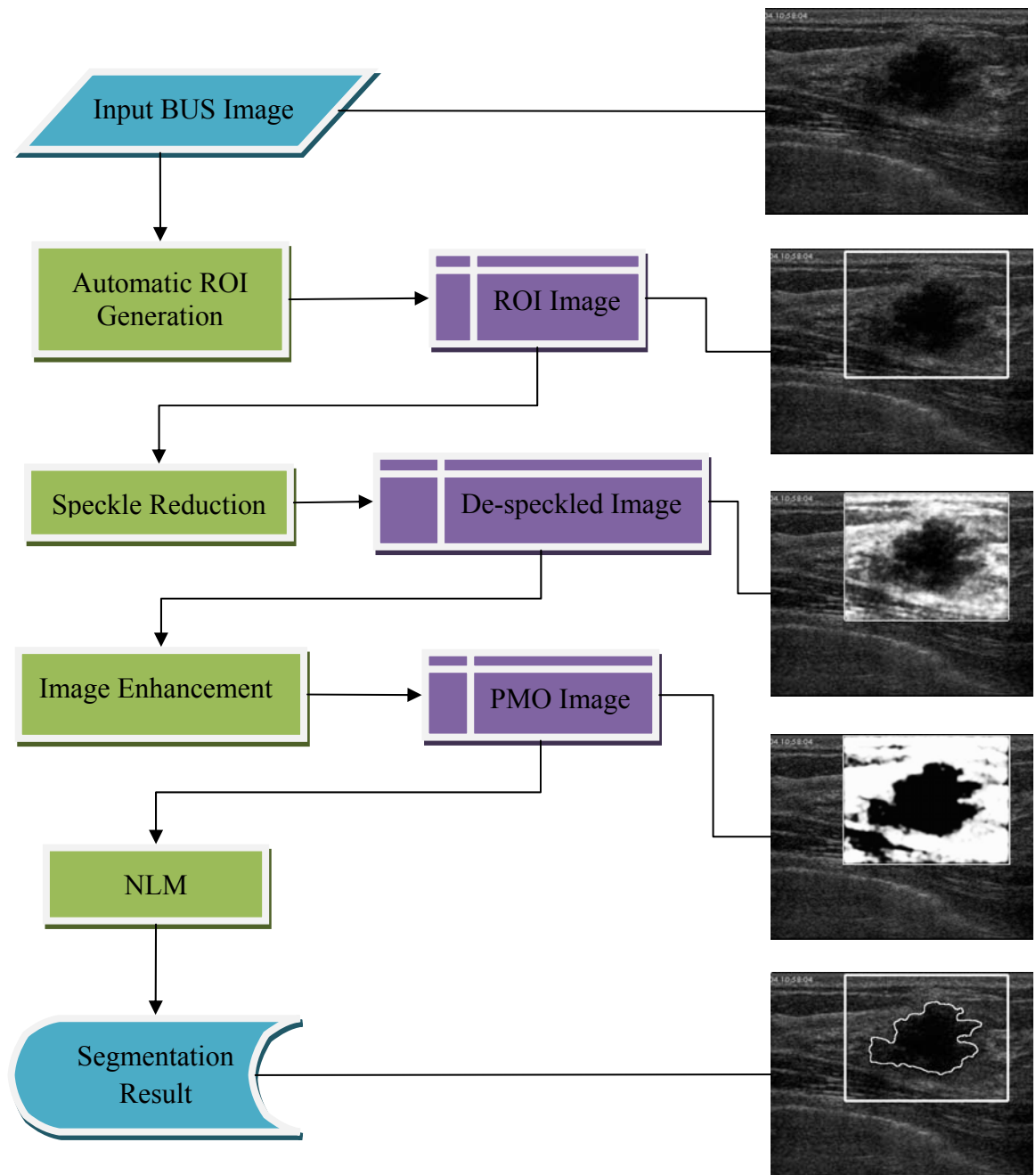


Figure 1.2. Flowchart of the proposed method.

3. An effective enhancement method for BUS images using phase information is proposed. Instead of using phase information as an edge detector as is commonly done, we propose a novel phase feature to enhance and smooth the lesion and background. The produced phase image (called a PMO image) has a more homogeneous foreground and background; and most important of all, the granular effect caused by speckle noise is greatly reduced.
4. A novel clustering method, neutrosophic *l*-means (NLM) based on neutrosophy and fuzzy c-means (FCM) is developed to separate the background and foreground of BUS images. Neutrosophy is a new branch of philosophy that has an excellent ability to deal with uncertainty. Said ability is fully employed to segment BUS images with vague boundaries. By defining neutrosophic components and incorporating an indeterminate degree in the clustering process, NLM can handle pixels with intermediate intensity values effectively. The clustering process is not only decided by the distance to the cluster centers and membership, but also by the indeterminate degree and neighborhood information.
5. A sound and fair comparison between different methods using the same database is conducted. In the experiment section, the proposed method is compared with FCM, and three other BUS image segmentation methods, using multiple evaluation metrics.

In Chapters 2-5, we describe each step of the proposed method. In Chapter 6, database and experimental results are discussed. Chapter 7 gives conclusion and future directions.

CHAPTER 2

AUTOMATIC REGION OF INTEREST GENERATION

Since BUS images contain a lot of different structures (connective tissue, fat, muscles, etc.) and the lesion area is usually small compared to the entire image, finding a region of interest (ROI) is quite helpful for improving the speed and accuracy of segmentation. Many existing BUS image segmentation methods have been developed based on a manually selected ROI, not on the whole image. Such a requirement impedes full automation. In this section, we describe the development of an automatic ROI generation method that facilitates full automation of BUS image segmentation.

There are two typical ROI definitions: one defines ROI as the rough contour or initial contour of the lesion, while the other defines ROI as a rectangular region containing both the lesion and some background information. In this work, the automatically generated ROI is a rectangular region. Therefore, this ROI generation method can be utilized by any other segmentation method as a preprocessing step since it only cuts the redundant background while keeping the lesion and nearby surrounding tissues untouched. The ROI generation method consists of two steps: automatic seed point selection and region growing. Region growing is chosen because it is simple and fast. The lesion boundary detected by the region growing method is usually not accurate on BUS images. However, the target here is only to roughly locate the lesion rather than find the accurate boundary. Therefore, region growing fits our needs very well.

2.1 Automatic Seed Point Selection

A seed point is the starting point for region growing. Its selection is important to the segmentation result. If a seed point is selected outside the region of interest (ROI), the final segmentation result would definitely be incorrect. Due to the low quality of US images, most region growing methods require the seed point be selected manually in advance. In order to make the region growing fully automatic, it is necessary to develop an automatic seed point selection method for BUS images. However, very little research has been done in this area; thus, relevant work is rare and immature. Poonguzhali and Ravindran [51] proposed an automatic method to select seed point for masses using both the co-occurrence and run length features. The run length features were calculated around the points selected by the co-occurrence features. If all the run length features of a selected point and its neighborhood points were equal, the point was considered as a seed point. In [21], after several preprocessing steps, a seed point score formula was used to evaluate a set of randomly selected points. The point with the highest score was considered as the seed point. In yet another method [52], after preprocessing and morphological operations, a binary image was obtained and the sum of the pixels on each row and column are computed. Indexes of the seed point were found as the row and column number with the max sums, respectively. All the aforementioned methods took into account only the statistics of the texture features for a mass region (i.e., the mass is darker than the surrounding tissues and more homogeneous than other regions). They failed to consider spatial features of a US mass (such as the fact that a mass frequently appears at the upper part of image and is barely connected with the image boundary).

Therefore, the probability of a selected seed point outside the lesion is high, especially in noisy and low-contrast images.

In this subsection, we develop a new automatic seed point selection method for BUS images [53]. The method not only considers the texture features of a lesion, but also incorporates the spatial characteristics of a lesion. We describe our method in details in Section 2.1.1. The new method is compared with the automatic seed point selection method in [21] using the same database in Section 2.1.2.

2.1.1 The Proposed Seed Point Selection Algorithm

Step 1: Speckle reduction. We employ the speckle reducing anisotropic diffusion (SRAD) [50] as the de-speckle method. SRAD can iteratively process a noisy image with adaptive weighted filters, reduce noise and preserve edges. The diffusion coefficient is determined by:

$$c(q) = \frac{1}{1 + [q^2(x, y; t) - q_0^2(t)] / [q_0^2(t)(1 + q_0^2(t))]}, \quad (1)$$

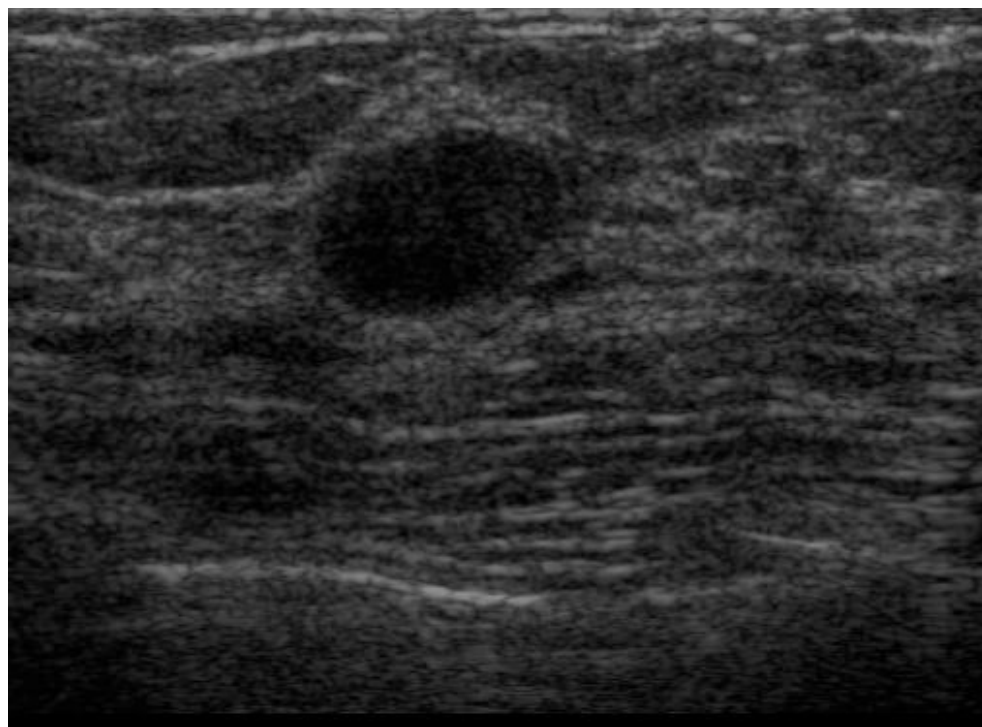
and the instantaneous coefficient is:

$$q(x, y; t) = \sqrt{\frac{(1/2)(|\nabla I|/I)^2 - (1/4^2)(\nabla^2 I/I)^2}{[1 + (1/4)(\nabla^2 I/I)]^2}}. \quad (2)$$

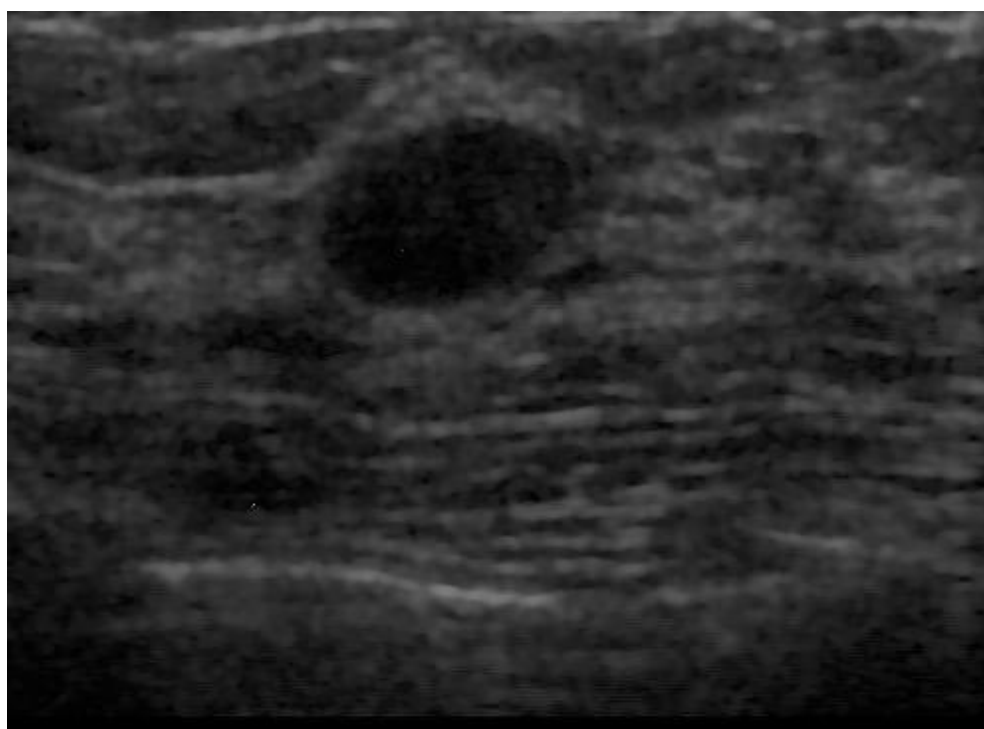
The initialized $q_0(t)$ is given by:

$$q_0(t) = \frac{\sqrt{\text{var}[z(t)]}}{z(t)}, \quad (3)$$

where $z(t)$ is the most homogeneous area at t . In our experiments, we set the iteration times as 5. Figure 2.1 shows the speckle reduction effect on the original BUS image.



(a)



(b)

Figure 2.1. (a) Original image. (b) Result after speckle reduction using SRAD [50].

Step 2: Iterative threshold selection. Most segmentation methods need to threshold the image into background and foreground. The threshold selection greatly affects the final segmentation result. Here, we iteratively select thresholds based on the histogram and breast lesion's spatial characteristics. No training or empirical-based threshold value is needed. The advantage of this iterative method is that it can be used for a BUS image without any requirement for image resource consistence or human interaction to tune a reasonable threshold value. Only information regarding the current BUS image is needed to determine the proper threshold.

We first calculate all the local minimums of the image histogram. A good threshold that can properly separate the lesion from the background should be one of these local minimums. Starting from the smallest to biggest, we evaluate every local minimum until we find the proper one. The iteration is described below:

1. Let t equal the current local minimum of the histogram. Binarize and reverse the de-speckled image using threshold t (lesion becomes white and background black) to get I_b . If the ratio of the number of foreground points and the number of background point is less than 0.1, let t equal the next local minimum. Continue until the ratio is no less than 0.1.
2. Perform dilation and erosion on I_b to remove noise.
3. Find all the connected components in I_b . If none of the connected components has an intersection with the image center region (a window about one-half the size of the whole image and centered at the image center), let t equal the next local

minimum. Continue until there is a connected component that has an intersection with the center window.

After the above procedures, a proper threshold t is chosen to binarize the image into background and foreground. Because the iterative threshold choosing process starts from the smallest local minimum and increases gradually based on the possible lesion to image ratio, it can avoid problems such as the foreground being too large (lesion is connected with other tissues) or too small (lesion is not included into the foreground). Figure 2.2 (a) illustrates the result of thresholding the image by the iteratively selected threshold.

Step 3: Deleting the boundary-connected regions. After image binarization, morphological operations are employed to remove noise regions. Then all the connected components are labeled again. Each connected component represents a possible lesion region. Besides the real lesion region, there are some regions connected with the boundary and such kind of boundary-connected regions always have a big area. We cannot simply delete all the regions connected with boundary of the image because sometimes the lesion region is also connected with the boundary. Therefore, we use the center window to evaluate every boundary region. The center window is about 1/2 size of the whole image and centered at the image center. If a region has no intersection with the center window and it is connected with the image boundaries, this region is deleted from the lesion candidate list. Figure 2.2 (b) shows the result of boundary region deletion.



(a)



(b)

Figure 2.2. (a) Result after iterative threshold selection. (b) Result after deleting boundary-connected region.

Step 4: Rank the regions. Now the left regions are either not connected with the boundary or they have an intersection with the image center window. We use the following score formula to rank each left region. The one with the highest score is considered as the lesion region.

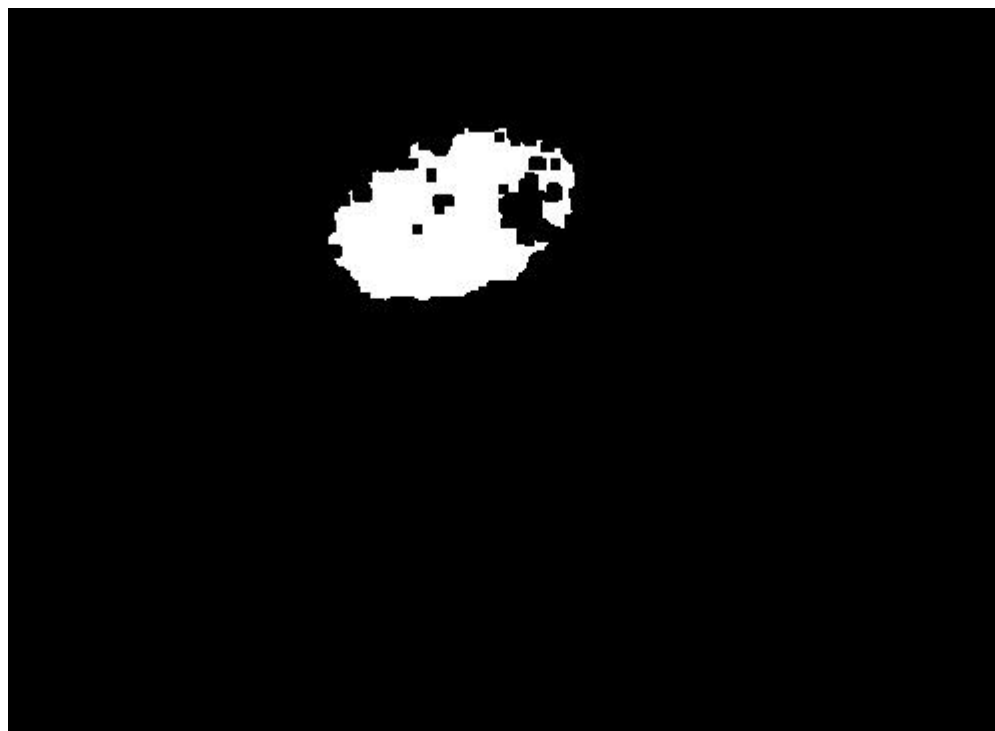
$$S_n = \frac{\sqrt{Area}}{dis(C_n, C_0) \cdot var(C_n)}, n = 1, \dots, k \quad (4)$$

where k is the number of regions, $Area$ is the number of pixels in the region, C_n is the center of the region, C_0 is the center of the image, and $var(C_n)$ is the variance of a small circular region centered at C_n .

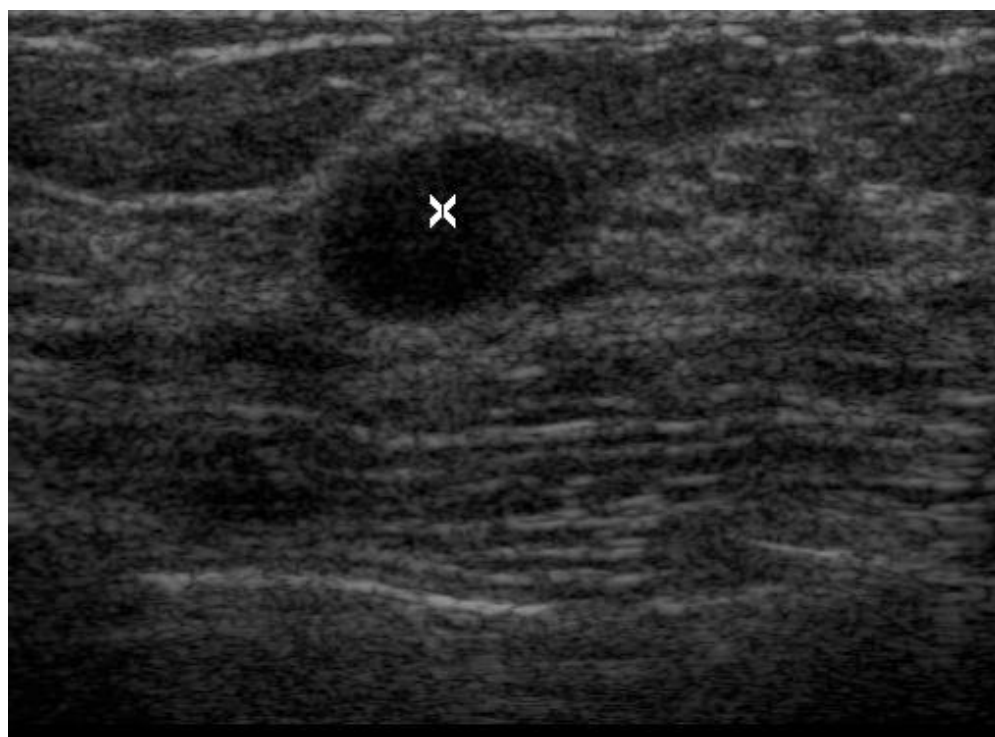
Step 5: Determine the seed point. Suppose the minimum rectangle contains the winning region $[x_{min}, x_{max}; y_{min}, y_{max}]$. For most cases, the center of the winning region $((x_{min}+x_{max})/2, (y_{min}+y_{max})/2)$ could be considered as a seed point. However, there are cases in which the lesion shape is irregular, and thus the center point might be outside the lesion. For these special cases, we choose a seed point by the following rule:

$$\begin{cases} x_{seed} = (x_{min} + x_{max}) / 2 \\ y_{seed} = \{\forall y \mid (x_{seed}, y) \in \text{lesion region}\} \end{cases} \quad (5)$$

Figure 2.3(a) illustrates the winning region, while Figure 2.3 (b) illustrates the final selected seed point on the original image.



(a)



(b)

Figure 2.3. (a) The winning region. (b) Selected seed point.

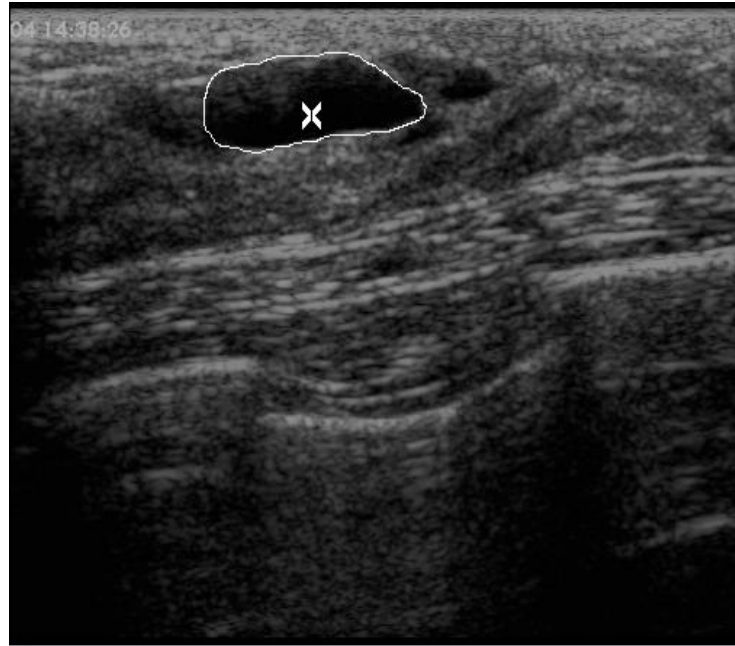
2.1.2 *Experiment Results of the Seed Point Selection Algorithm*

The proposed seed point selection method is tested using our BUS database. The database consists of 60 images with various breast lesions. Each lesion's boundary has been manually outlined by radiologists. More detailed information of the database is given in Section 6.1. As long as the detected seed point is inside the lesion, we consider such case as a true positive (TP). On the other hand, if the seed point is outside the manually outlined lesion or on the boundary, we count it as a false positive (FP).

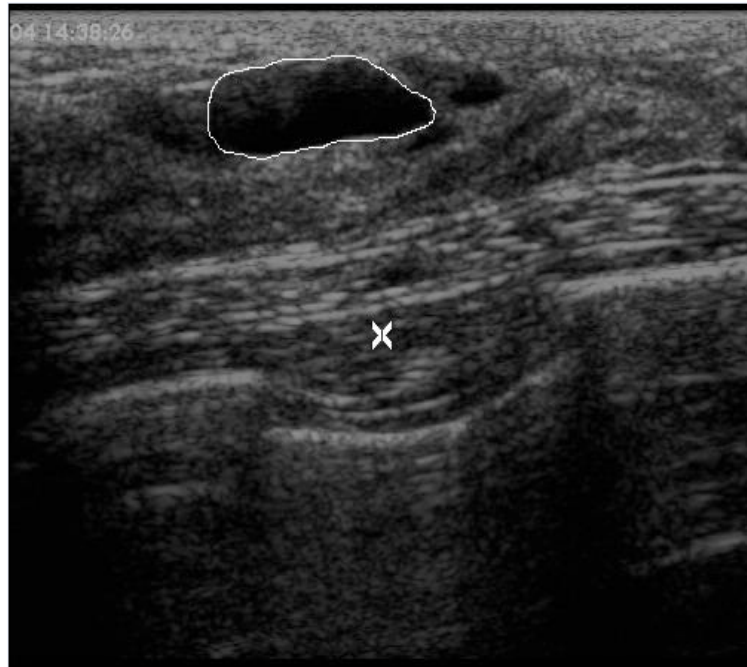
Furthermore, we separate TP cases into two categories: seed point in the center part of the lesion and seed point near the boundary. Although these two categories are not strictly distinguished from each other, we can use statistical values to evaluate the quality of the seed point selection method, given the assumption that the closer the seed point is to the center of the lesion, the better the seed point is.

Next, we compared our method with the automatic seed point selection method in [21]. Seed point selection is one step of the low level processes in the segmentation system developed in [21]. The method needs to calculate the pdfs for intensity and texture on a training set before seed point selection. To maximize the performance of the method in [21], we use all 60 images in the database to train the pdfs, and then use the same 60 images to test the method. The performance comparison is given in Table 2.1. Figure 2.4 gives two example results of our method and the method in [21].

Based on the experiment results, the proposed algorithm outperforms the seed point selection algorithm in [21], not only on accuracy, but also on the seed points' quality. As we mentioned above, the more a seed point is near the center of the lesion, the better the

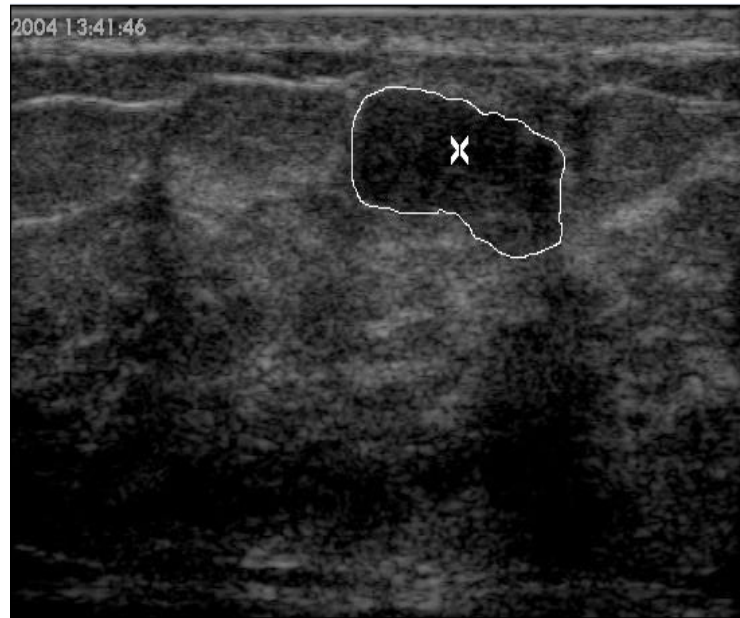


(a)



(b)

Figure 2.4. Results of two cases: (a) and (c) are the results of the proposed seed point selection algorithm; (b) and (d) are the results of the seed point selection algorithm in [21]. (Continued on next page.)



(c)



(d)

Figure 2.4. (cont.) Results of two cases: (a) and (c) are the results of the proposed seed point selection algorithm; (b) and (d) are the results of the seed point selection algorithm in [21].

Table 2.1. Comparison of the Proposed Seed Point Selection Algorithm and the Active Contour Method [21].

Method	FP	TP	
		Seed point near center	Seed point near boundary
Seed point selection method in [21]	16 (26.67%)	35 (58.33%)	9 (15.00%)
The proposed seed point selection method	0 (0%)	51 (85.00%)	9 (15.00%)

seed point is for region growing. Therefore, the percentage of seed points with good quality found by the proposed algorithm is much higher than that of the algorithm in [21]. The percentage of good seed points by the proposed algorithm is 85% and by algorithm in [21] is 58.3%.

2.2 Region Growing

After a seed point is generated automatically, we employ a region growing method to obtain a preliminary lesion boundary. Region growing is a frequently used segmentation method in medical image processing. Its main advantage is its fast processing speed, while its main disadvantage is that the method cannot guarantee accurate boundary detection for BUS images. The reason we choose region growing here is that we only need a rough contour to estimate the ROI borders; therefore, we do not employ any complicated algorithm but use region growing to save overall processing time.

The basic criterion of region growing for a simple segmentation task is to compare the intensity value of the new pixel v with the intensity mean of the current region, and if

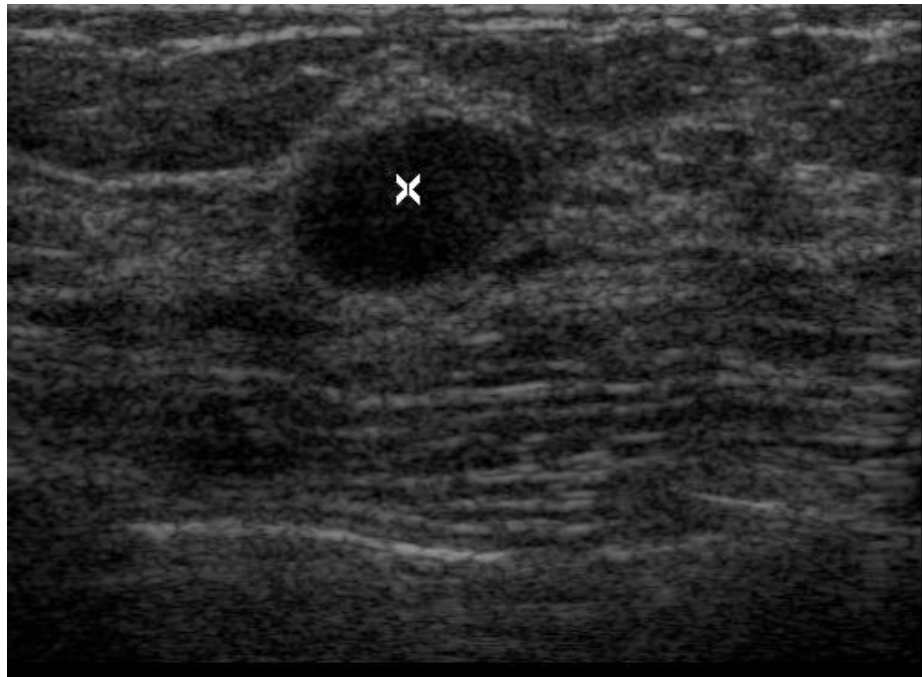
they are close enough, pixel v is added into the region. However, it is not enough to use only the intensity mean of the current region to control the growth process for a BUS image. We find the stop criterion is related to both the intensity mean of the current region and the intensity mean of the overall image. Therefore, the following conditions are used to control the growing process. Let R represent the set containing all the pixels in the region, and p be a pixel in R . At the beginning, set R contains only the seed point S_0 . A pixel v is included in R , if $\exists p \in R$ and satisfies the following condition:

$$\{G(v) \leq \max(\frac{M}{b_2}, \min(b_1 \times m, M))\} \text{ and } \{N(p) \cap N(v) \neq \emptyset\} \quad (6)$$

where $G(v)$ is the intensity value of pixel v , m is the intensity mean of region R , M is the intensity mean of the whole image, and b_1 and b_2 are the parameters tuning the relationship between the stop criterion and the intensity means of the current region and the overall image. N denotes the type of connectivity of the neighborhood pixels around the pixel under consideration. The above operation proceeds until no more pixels satisfying Eq. (6) remain. In this work, we used 8-neighborhood connectivity. $b_1=1.5$ and $b_2=1.6$ are determined by experiment.

Based on the region growing result, a rectangular ROI is located from the original image. To make sure that the lesion is completely covered by the ROI, we let the rectangular region have a 50-pixel expansion surrounding the region growing result. For example, suppose the size of the original image is 500*600 as shown in Figure 2.5(a), with the lesion area obtained from the region growing area as [150:200, 250:350] (see Figure 2.5(b)), then the rectangular region [100:250, 200:400] is finally chosen as the ROI (Figure 2.5(c)). In our experiments, the average processing time for ROI generation

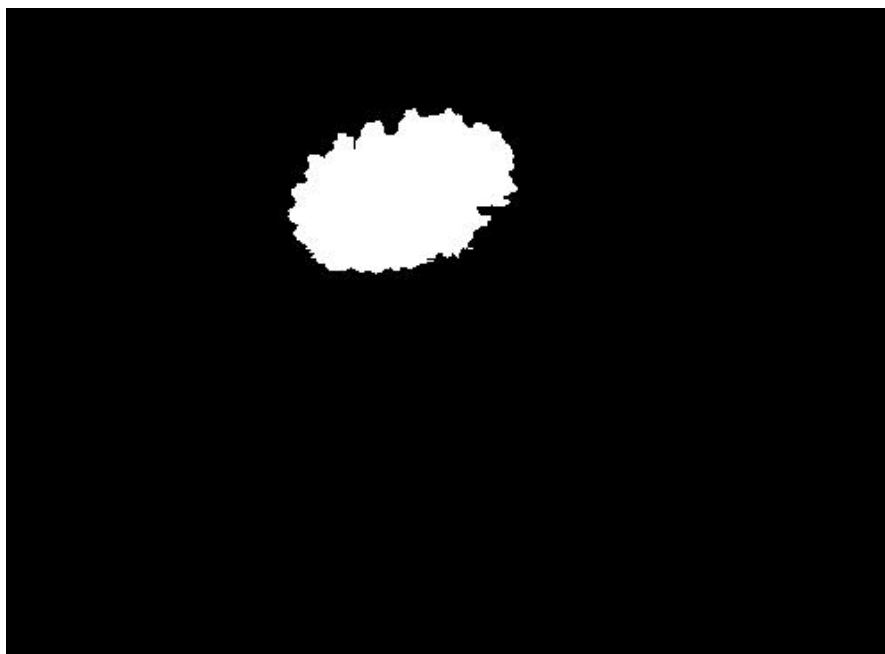
for each case is 1.97 seconds, using a 3.0 GHz Pentium processor (0.36 seconds for seed point selection and 1.61 seconds for region growing).



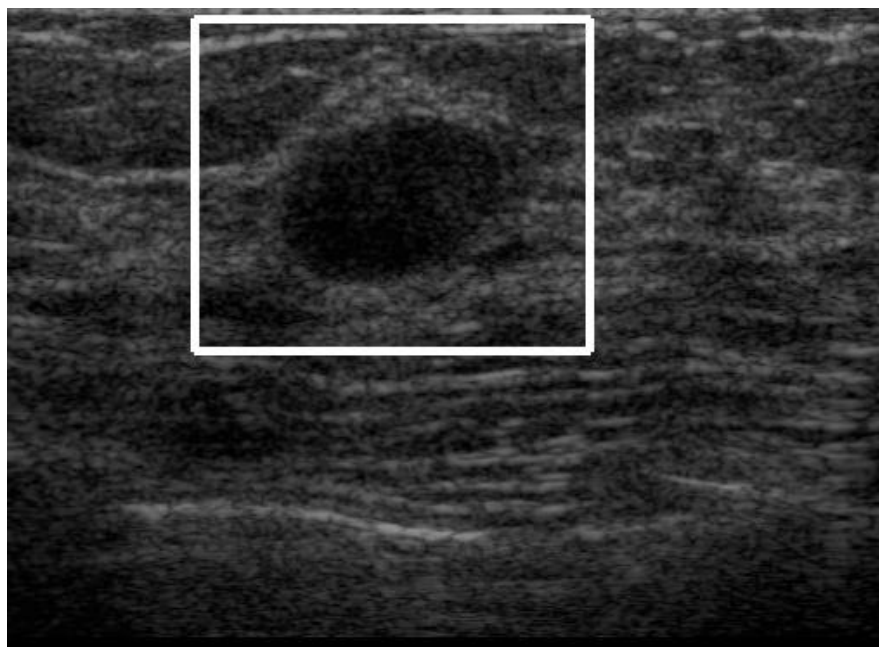
(a)

Figure 2.5 (a) Original image with seed point marked. (b) Result of region growing.

(c) ROI. (Continued on next page.)



(b)



(c)

Figure 2.5. Cont. (a) Original image with seed point marked. (b) Result of region growing.

(c) ROI.

CHAPTER 3

SPECKLE REDUCTION

Speckle is an inherent characteristic of ultrasound imaging. It takes the form of multiplicative noise generated by a number of scatterers with a random phase within the resolution cell of an ultrasound beam [54, 55]. The texture of the observed speckle pattern does not correspond to the underlying structure. The local brightness of the speckle pattern, however, does reflect the local echogenicity of the underlying scatterers. There are generally two contrary opinions about speckle. One opinion insists that speckle is solely noise to an ultrasound image and should be removed, since speckle significantly degrades the image quality, hence making it more difficult for the observer to discriminate the fine detail of images [56, 57]. This opinion is commonly accepted. The other opinion argues that speckle patterns reflect the local echogenicity of the underlying scatters which means speckle has underlying useful characters rather than merely being noise [18]. However, very little work has been done to explore the underlying characters of speckle.

In this work, we treat speckle as noise and try to suppress speckle without destroying important features of the lesions. Two effective de-speckle methods are taken into consideration. One is the speckle reducing anisotropic diffusion (SRAD) [50], and the other is a newly published de-speckle method [58]. Both of the methods are good at removing the speckle noise and preserving the edges and details of the images at the same time. SRAD is a diffusion method in which the diffusion is edge-sensitive for speckled images. Its advantage is high speed and a good de-speckle effect. Anisotropic

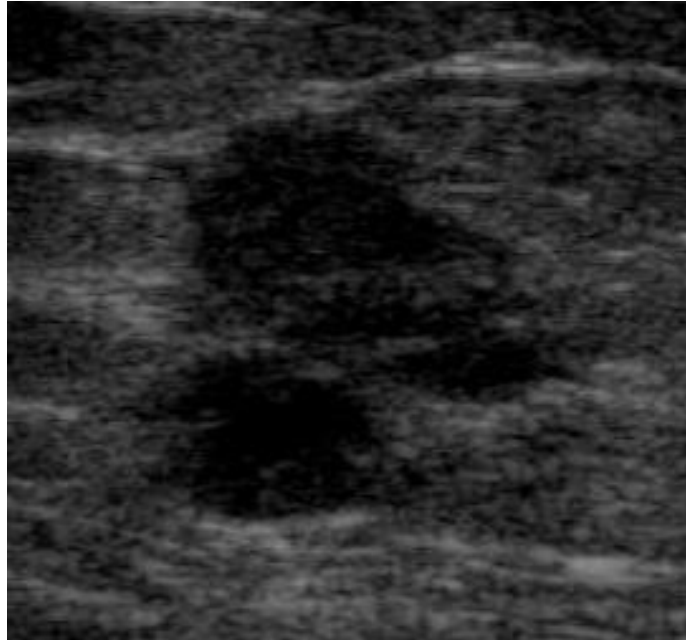
diffusion is frequently used in filtering techniques for speckle reduction. However, edge estimation using a gradient operator makes it difficult to handle a multiplicative noisy image. In order to eliminate such a disadvantage, SRAD is proposed particularly for envelope US images without logarithmic compression. In SRAD, the instantaneous coefficient of variation serves as the edge detector. The function exhibits high values at edges and produces low values in homogeneous regions. Thus, it ensures the mean-preserving behavior in the homogeneous regions, and edge-preserving and edge-enhancing at the edges.

The method in [58] is a speckle reduction method tailored especially for BUS images. It uses the local homogeneity defined by texture information to describe speckle noise. A 2-D homogeneity histogram is built, and the threshold is obtained using the maximal entropy principle. The pixels are divided into a homogenous set and a non-homogenous set based on the homogeneity threshold. The pixels in the non-homogeneous set are handled by the proposed directional average filters (DAF) iteratively.

Figure 3.1 shows the results of the two methods. Obviously, the edges are better enhanced, and speckle noise is more effectively reduced by the method in [58] than the SRAD in [50]. Here a quantitative evaluation metric, the signal-to-mean square error (*SMSE*), is employed to evaluate the de-speckle effect [59]:

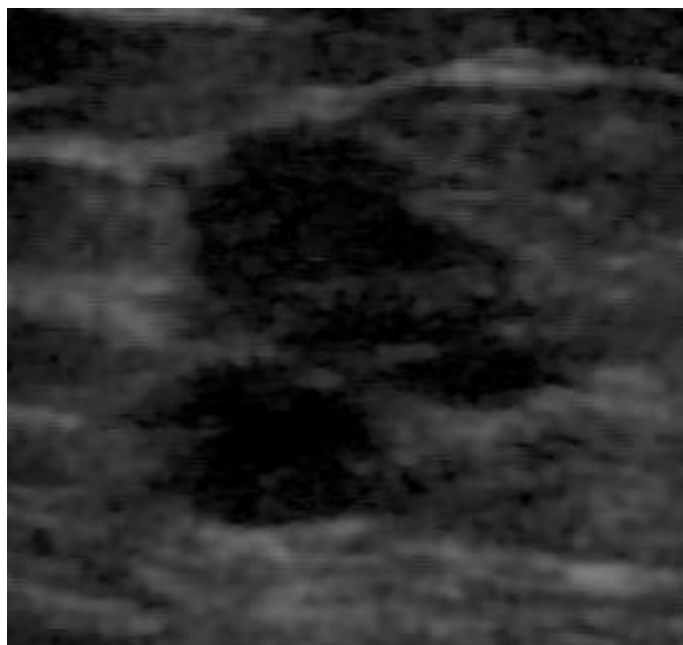
$$SMSE = 10 \log_{10} \left(\frac{\sum_{i=1}^K S_i^2}{\sum_{i=1}^K (\hat{S}_i - S_i)^2} \right) \quad (7)$$

where S_i is the i th pixel in the original image (speckle-free image), \hat{S}_i is the i th pixel in the image after speckle reduction and K is the image size. A larger $SMSE$ ratio means a better noise suppression effect. Since there is no speckle-free ultrasound image in reality; we use the method in [60] to approximate the speckle-free images by a homomorphic Wiener filter.

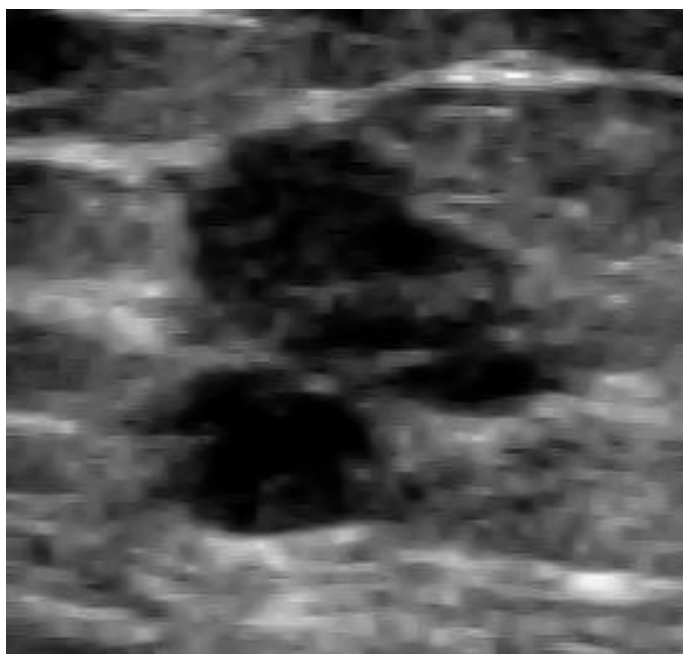


(a)

Figure 3.1. (a) The ROI cut from the original image. (b) Result of SRAD [50] after 5 iterations. (c) Result of the method in [58]. (Continued on next page.)



(b)



(c)

Figure 3.1. Cont. (a) The ROI cut from the original image. (b) Result of SRAD [50] after 5 iterations. (c) Result of the method described in [58].

A comparison between the two methods is conducted on the whole database. Both the de-speckle effect and time complexities are analyzed. As Table 3.1 shows, the average *SMSE* ratio of the method in [58] is higher than that of the SRAD method (30.80 over 16.66), while the average processing time of the method in [58] is longer than that of SRAD. Considering that the processing time (about 8 seconds) is acceptable for clinical application and the de-speckle effect is much better, we choose the method in [58] as the speckle reduction algorithm here.

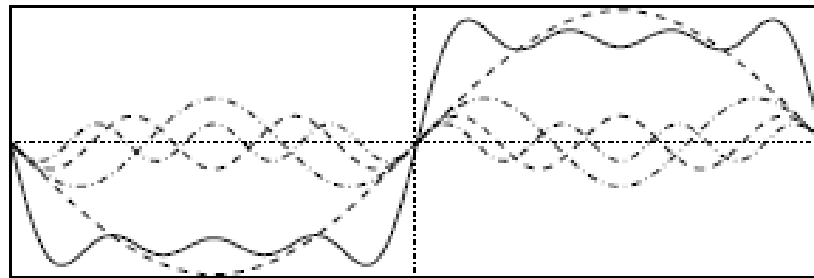
Table 3.1 Comparison of De-speckle Effect and Time Complexity of the Method
Described in [58] and SRAD in [50].

Methods	SMSE	Average processing time/case
De-speckle method in [58]	30.80	8.46 seconds
SRAD method in [50]	16.66	0.62 second

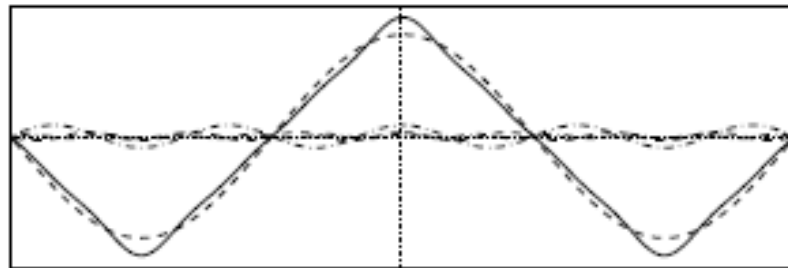
CHAPTER 4

IMAGE ENHANCEMENT USING LOCAL PHASE INFORMATION

Local phase information has been suggested as a robust feature for acoustic boundary detection [18]. It characterizes different intensity features in terms of the shape of the intensity profile rather than the intensity derivative. For example, at the point of the edge transition, all Fourier components are exactly in phase at zero or π depending on whether the step is upward or downward (Figure 4.1(a)). Similarly, for an intensity ridge, the



(a)



(b)

Figure 4.1 (a) Fourier series of a step edge. Dashed lines are the first four Fourier components and solid lines are the sum of these components [61]. (b) Fourier series of an intensity ridge. Dashed lines are the first four Fourier components and solid lines are the sum of these components [61].

phases of all Fourier components are $\pi/2$ at its peak (Figure 4.1(b)). The most important advantage of local phase is that it is invariant to image illumination and contrast, i.e., the local phase does not change no matter whether the contrast between foreground and background is low or high. Since acoustic image feature detection should be robust to speckle noise and low image contrast, measures based on phase information rather than intensity derivatives may be more appropriate for acoustic feature detection [62].

4.1 Local Phase 1-D Detection

To analyze the local phase feature of a 1-D signal, $I(x)$, a signal with step edges and intensity ridge (Figure 4.2(a)) is considered. A bank of Log-Gabor filters with increasing wavelengths is multiplied to the signal. Let M_s^e and M_s^o denote the even and odd symmetric Log-Gabor filters in quadrature at scale s . The original 1-D signal (with DC component removed) and its Hilbert transform can be approximated by [62]:

$$e(x) = \sum_{s=1}^n I(x) * M_s^e, \quad o(x) = \sum_{s=1}^n I(x) * M_s^o. \quad (8)$$

For each single scale, the local phase is defined as:

$$phase(x, s) = \|\tan^{-1}(e(x, s) / o(x, s))\| \quad (9)$$

where

$$e(x, s) = I(x) * M_s^e, \quad o(x, s) = I(x) * M_s^o. \quad (10)$$

The $e(x, s)$ and $o(x, s)$ are called the even and odd components of the signal at a given scale s .

It should be emphasized that when the phase is referred to in this dissertation, it is ‘local phase’ that is being considered, which is different from the ‘phase’ defined in the

frequency domain. Local phase is defined for each position x at the spatial domain after the signal is convolved with an analyzing filter (such as the Log-Gabor filter). Conversely, phase is obtained from the fast Fourier transform (FFT) of a signal which is defined as the phase offsets of the sinusoidal basis functions in the decomposition.

It is always confusing how to calculate M_s^e and M_s^o in the spatial domain. In real implementation, the above analysis is done in the Fourier domain by FFT since it is more convenient and fast to do convolution operations in the frequency domain. The signal is transformed by FFT, and then a bank of Log-Gabor filters is used to analyze the signal. The Log-Gabor filters are defined in the frequency domain as:

$$G(\omega) = \exp\left(-\frac{(\log(\omega / \omega_0))^2}{2(\log(\kappa / \omega_0))^2}\right), \quad (11)$$

where κ is related to the bandwidth of the filter and ω_0 is the center frequency of the filter.

The value κ / ω_0 ensures a constant shape-bandwidth ratio over scales. κ / ω_0 is set as 0.55 to get a compromise between filters compact and avoiding aliasing effect [62].

After being analyzed by the filters with different scales, the original signal is decomposed into a group of sub-signals, while each sub-signal is a copy of the original signal after filtering with a Log-Gabor filter with a special scale. If the bank of Log-Gabor filters has 64 scales, 64 sub-signals are obtained and each sub-signal picks out a special frequency of the original signal. Then, the group of sub-signals is transformed back to the spatial domain by an inverse fast Fourier transform (IFFT). Let $I'(x, s)$ be the signal transformed back from the Fourier domain at scale s . Local phase can be calculated by:

$$phase(x, s) = || \angle(I'(x, s)) || = || \tan^{-1}(\text{imag}(x, s) / \text{real}(x, s)) || \quad (12)$$

where $\text{imag}(x, s)$ is the imaginary part of the $I'(x, s)$ and $\text{real}(x, s)$ is the real part of the $I'(x, s)$.

If we plot the local phase vectors one-by-one along the x dimension, a phase scalogram can be derived for better observation of the phase features across different scales. Figure 4.2(a) is a 1-D signal $I(x)$. In Figure 4.2(b), the local phase scalogram is plotted for distance x along the signal over a range of scale s . Black is the zero phase and white is the π radians. Please note that when local phase is calculated by Eq. (12), the absolute operator is utilized; therefore, both the positive edge and the negative edge correspond to π radians, and intensity ridge corresponds 0 phase. Observe that, at the step edge labeled as 1 and 2 in Figure 4.2(a), the corresponding phase values in Figure 4.2(b) are consistent at π (shown as the white lines), no matter whether small scales or large scales. At the intensity ridge labeled as 3 in Figure 4.2(a), the phase values in Figure 4.2(b) are consistent at 0 (shown as the black line). Based on such observations, if one accumulates all the local phases at different scales, the highest peaks should represent step edges and the lowest valley should represent the intensity ridge. The definition of local phase accumulation (LPA) is given as:

$$LPA(x) = \frac{1}{n} \sum_{s=1}^n phase(x, s) \quad (13)$$

where n is the total number of scales, $phase(x, s)$ is the local phase defined in Eq. (12). Figure 4.2(c) plots the LPA with the corresponding step edges 1 and 2, and intensity ridge 3 labeled.

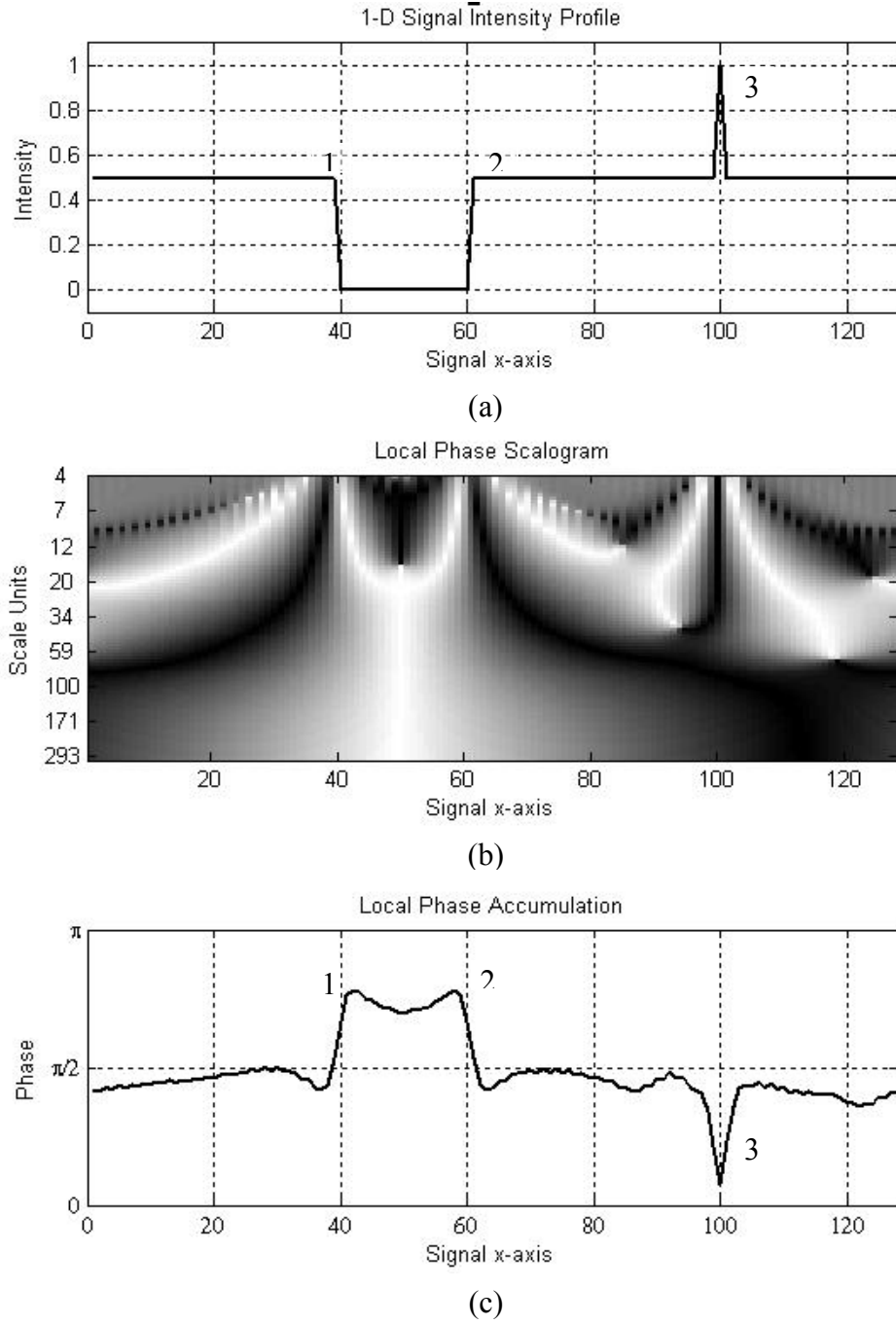


Figure 4.2 (a) A 1-D signal with step edges (1, 2) and intensity ridge (3). (b) Local phase scalogram obtained by a bank of Log-Gabor filters. (c) Local phase accumulation by adding up the above local phase scalogram and divided by the total number of scales.

A more interesting phenomenon is observed when taking a more detailed view of the local phases at different scales. In the local phase scalogram plotted in Figure 4.2, the total number of scales is 90 (90 Log-Gabor filters are used), and the wavelength of the Log-Gabor filters ranges from 4 to 323. From these scales, we picked out several samples and plotted the local phase profiles at the sample scales in Figure 4.3. Notice that the step edges in the original signal (labeled 1 and 2) correspond to the consistent $\pi/2$ in the local phase profiles across different scales (marked by small red circles). In the same way, the intensity ridge (labeled 3) in the 1-D signal corresponds to the consistent 0 in the local phase profiles across different scales (marked by small blue circles). Besides the edge and intensity ridge structures, no other point in the original signal remains consistent throughout the different local phase profiles. Such consistency for the edges and intensity ridge is kept very well when the wavelength of the Log-Gabor filters is within some predefined range. When the wavelength of the filters is too large, the consistency is broken. As the last plot in Figure 4.3 shows, when the scale number = 60 and the wavelength = 74.7, the local phase consistency at $\pi/2$ per step edge has moved up to about $3\pi/4$, and the local phase for intensity ridge has moved up, too. In other words, local phase consistency is only kept well if the frequency of analyzing filters falls into a certain range. If too large a range is chosen, the consistency is weakened.

Based on the above analysis, we cut the total scales of the bank of Log-Gabor filters from 90 to 45. The range of wavelengths therefore is between [4, 36]. Then, we plot the new LPA shown in Figure 4.4 for the same original 1-D signal. Compared with Figure

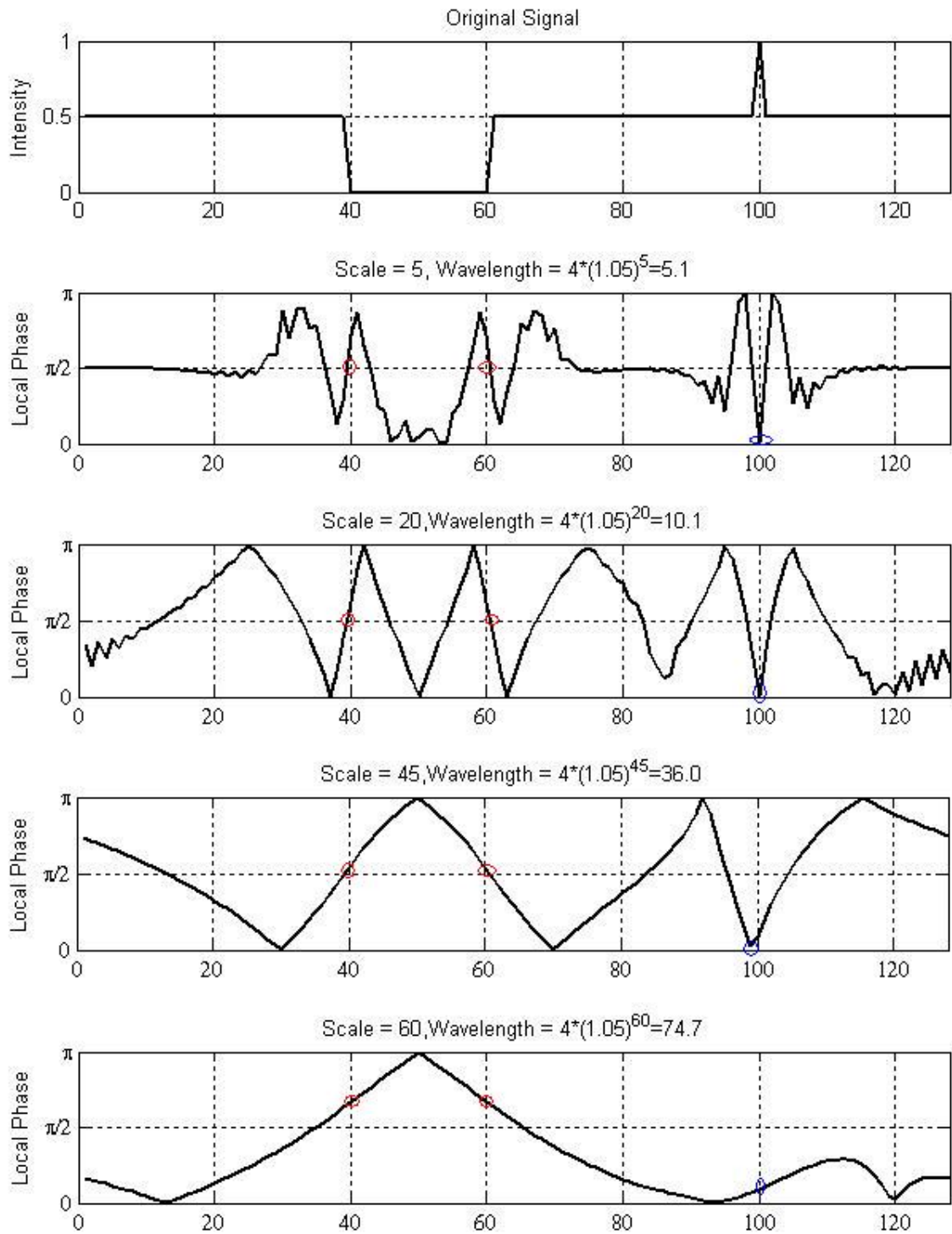


Figure 4.3. Local phase profiles at different scales.

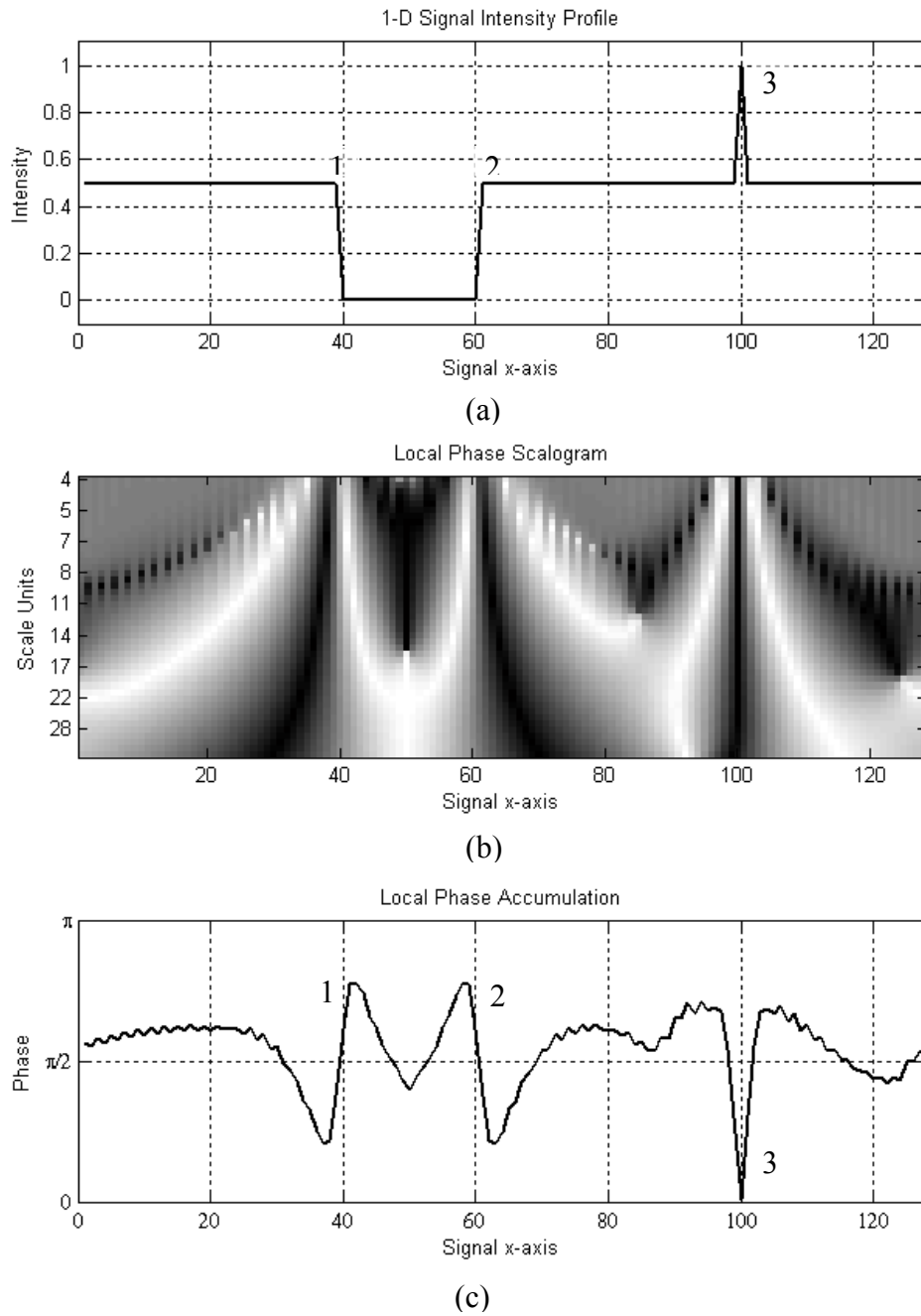


Figure 4.4 (a) A 1-D signal with step edges (1, 2) and intensity ridge (3). (b) Local phase scalogram obtained by a bank of Log-Gabor filters (max wavelength = 36.0). (c) Local phase accumulation by adding up the above local phase scalogram and divided by the total number of scales.

4.3(c), the peaks (corresponds to step edges) and the valley (corresponds to intensity ridge) in the LPA profile are more distinguishable.

Since only the local phases of a step edge and an intensity ridge at different scales keep consistency at $\pi/2$ and 0, respectively, the edges can be strengthened and intensity ridges can be weakened based on their distinguished features in local phase. In an ultrasound image, the boundary of a lesion is similar to the step edges and noise is similar to the intensity ridge [61]; therefore, we need a function that can strengthen phase at $\pi/2$ and weaken phase at 0. The cosine function is employed here:

$$phase' = [\pi - \pi * \cos(2 * phase)] / 2 \quad (14)$$

where θ is the local phase. The function is plotted in Figure 4.5. After the edge-strengthening function, the range of local phase is not changed (still between $[0, \pi]$) but the values at $\pi/2$ (for step edges) are strengthened, and values at 0 (for intensity ridges) are weakened.

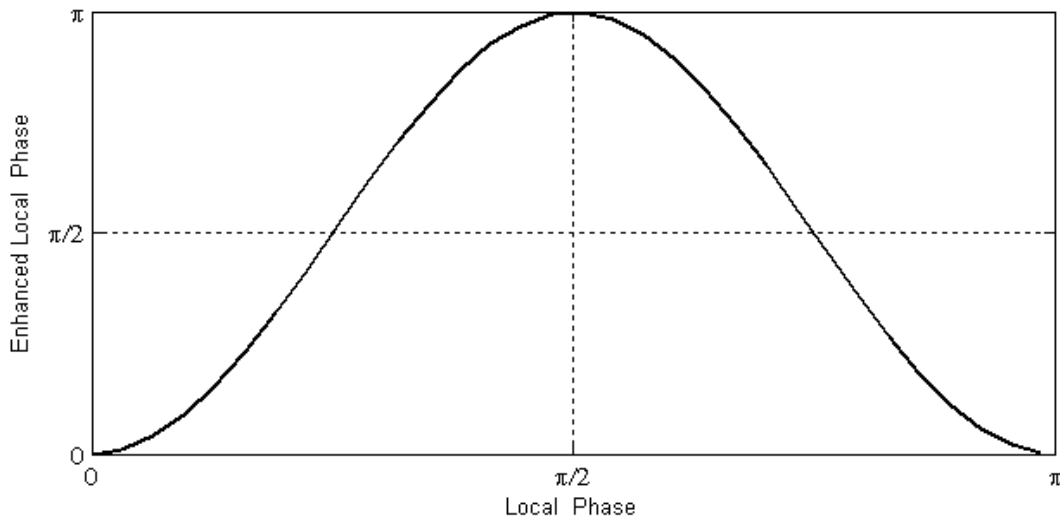


Figure 4.5. Local phase strengthening function (Eq. (14)).

After the local phase at every scale is enhanced by the strengthening function, LPA is recalculated by:

$$LPA'(x) = \frac{1}{n} \sum_{s=1}^n phase'(x, s) \quad (15)$$

where n is the total number of scales, $phase'(x, s)$ is the enhanced local phase defined in Eq. (14). The original LPA and enhanced LPA' are plotted in Figure 4.6.

4.2 From 1-D Signal to 2-D Image

To detect features in images, the above analysis of local phase needs to be extended from 1-D to 2-D. One solution is to calculate local phase in a number of separate orientations and combine the information to get a single measurement.

A bank of 2-D Log-Gabor filters is applied to the image in the frequency domain. The 2-D Log-Gabor filter in a given orientation θ_0 is defined as the 1-D Log-Gabor filter multiplied by a Gaussian orientation function [62]:

$$G(\omega, \theta) = \exp\left(-\left(\frac{(\log(\omega / \omega_0))^2}{2(\log(\kappa / \omega_0))^2} + \frac{(\theta - \theta_0)^2}{2\sigma_\theta^2}\right)\right) \quad (16)$$

where σ_θ defines the spread of the Gaussian orientation function centered at θ_0 . In this work, 6 orientations (0° , 30° , 60° , 90° , 120° , 150°) are chosen because they achieve a good compromise between a complete coverage of the whole spectrum and efficiency. The orientation spread σ_θ is set as 30° . The implementation has refers to Kovessi's Matlab code in [63].

Based on the observation on the 1-D signal's phase scalogram, the local phases keep consistent at $\pi/2$ for step edges and 0 for intensity ridge. LPA can pinpoint such

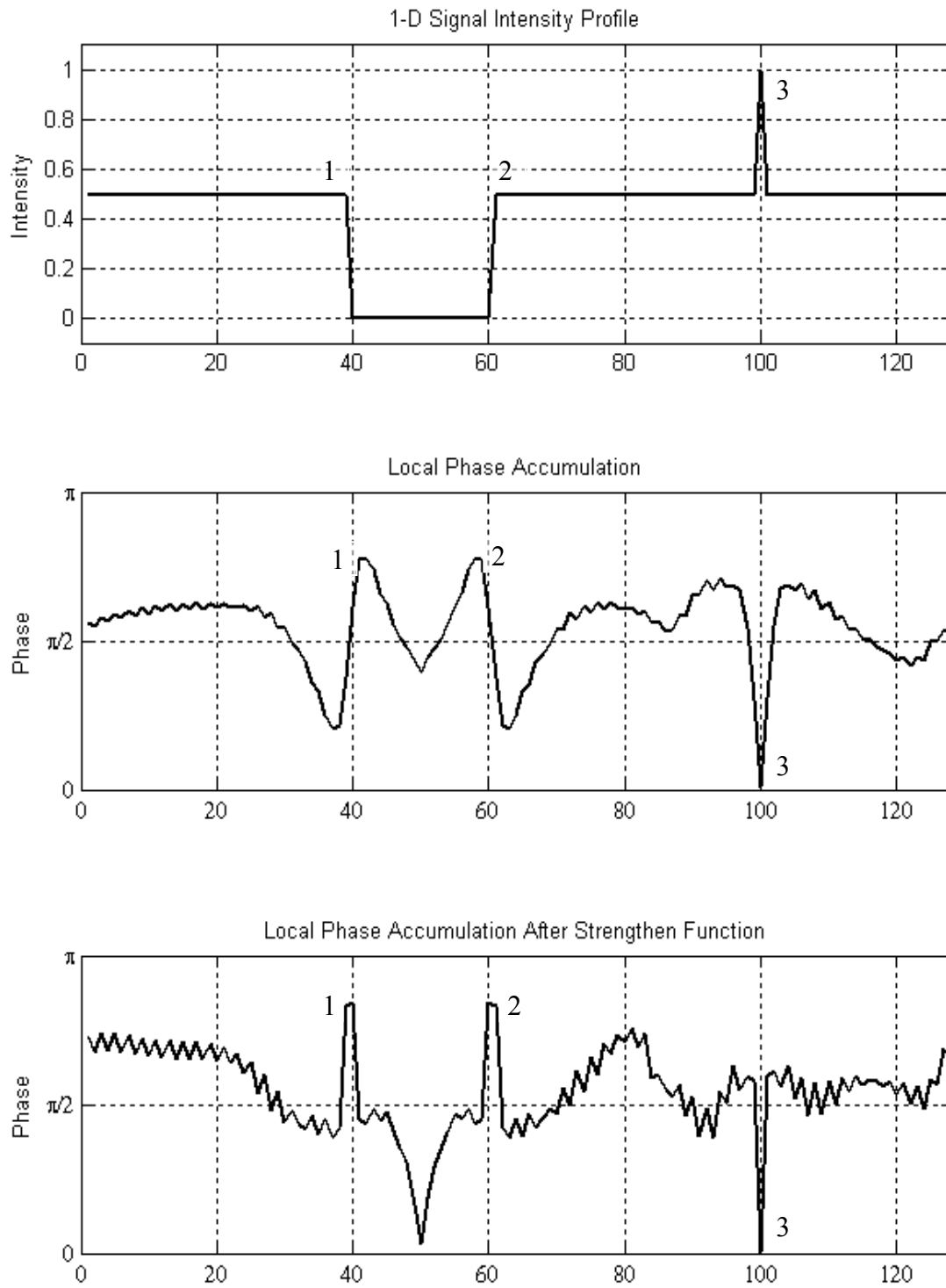


Figure 4.6. L before and after the strengthening function (Eq. (14)).

consistency. In a 2-D image, the LPA has the same characteristics. The only difference is that there are 6 LPAs since the image is filtered in 6 orientations. 2-D local phase accumulation LPA_θ for a single orientation is defined as:

$$LPA_\theta = \frac{1}{n} \sum_{s=1}^n phase'(s) \quad (17)$$

where θ is the orientation, n is the total number of scales, $phase'(s)$ is the enhanced local phase matrix at scale s by Eq.(14).

As for each orientation, there is a LPA feature matrix; after filtering in 6 orientations, there are 6 LPA feature matrixes. How to combine the 6 phase features into a single feature is our next task.

The commonly employed combination method is adding up the phase features for all the orientations, then using the summation to pinpoint image features:

$$SumPhase(i, j) = \sum_{\theta} LPA_\theta(i, j), \quad \theta = 0^\circ, 30^\circ, 60^\circ, 90^\circ, 120^\circ, 150^\circ \quad (18)$$

In this work, we propose a new aspect to solve the above problem. It is that the phase from the orientation with maximum corresponding energy might provide better image features than the phase summation from all the orientations. This is because unlike the 1-D signal, in a 2-D image, the edge has orientation information, and different parts of the edge or boundary might have different orientations. Therefore, the LPA in the direction of the edge might better characterize the structure than the summation of all the LPAs in different orientations. Since local energy characterizes structure information, the orientation with the maximum local energy should mostly approximate the direction of

the edge. Therefore, a novel 2-D phase feature PMO (phase in max-energy orientation) for every pixel (i, j) , is defined as:

$$PMO(i, j) = LPA_{\rho}(i, j), \quad \rho = \arg \max_{\theta=0^{\circ}, 30^{\circ}, 60^{\circ}, 90^{\circ}, 120^{\circ}, 150^{\circ}} Eng_{\theta}(i, j) \quad (19)$$

where LPA_{ρ} represents the matrix of local phase accumulation in orientation ρ and Eng_{θ} represents local energy in orientation θ . Local energy Eng_{θ} is calculated by:

$$Eng_{\theta} = \sqrt{\left(\sum_{s=1}^n e(s)\right)^2 + \left(\sum_{s=1}^n o(s)\right)^2} \quad (20)$$

where $e(s)$ and $o(s)$ are the even and odd components of the image after applying Log-Gabor filter at scale s .

The result of the above two ideas is shown on a clean image first. Figure 4.7(a) is the original image; (b) is the SumPhase feature image that is obtained by Eq. (18); (c) is the PMO feature image obtained by Eq. (19). As Figure 4.7 shows, PMO pinpoints the edge more clearly than SumPhase, i.e., the local phase from the orientation with maximum corresponding energy provides a better edge feature than the phase summation from all the orientations.

Next, the PMO feature image is calculated on a real BUS image. As Figure 4.8 shows, a ROI is first generated (Figure 4.8(a)) from the original BUS image, and the de-speckle method in [25] is used to suppress noise (Figure 4.8(b)). The PMO feature image (Figure 4.8(c)) for the real BUS image contains quite complicated information, including the edges of the lesion and background tissues. Here, we have a series of post-processing for the PMO feature image to make both the lesion and background homogeneous. The PMO image is first multiplied by the de-speckled ROI image to unify the lesion region (Figure

4.8(d)); then the PMO image is filtered with a 5×5 median filter three times to smooth the background (Figure 4.8(e)). After the above operations, the entire image becomes smoother and clearer, and the granular appearance is greatly reduced. However, most of the pixels are in the intensity range of $[0, 0.5]$; thus the whole image looks dark and dim. A brightening function in Eq. (21) is employed to adjust the intensity range to $[0, 1]$. To further increase the contrast between lesion and background, an intensification function in Eq. (22) is employed to make the bright pixels brighter and dark pixels darker. Therefore, the contrast between lesion and background is greatly enhanced (Figure 4.8(f)):

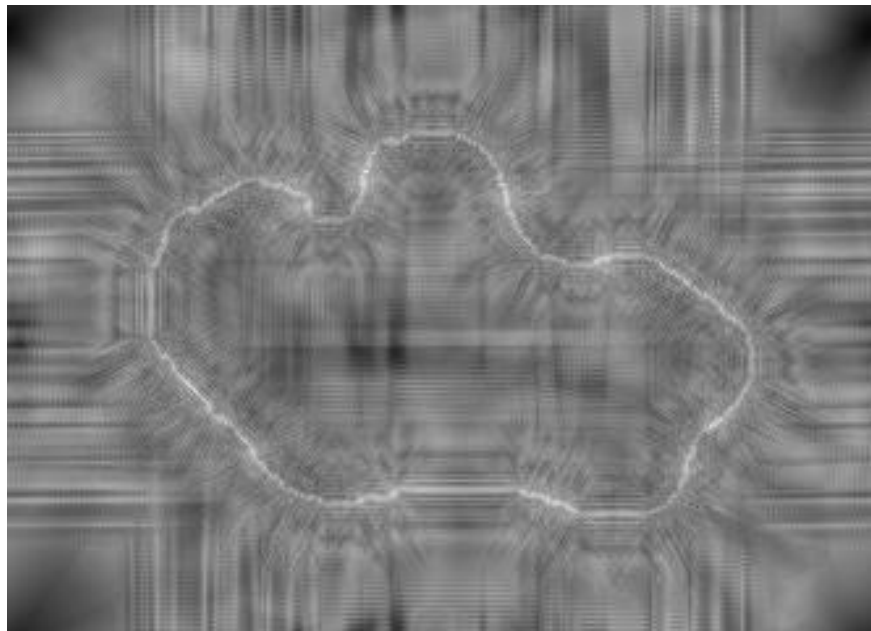
$$PMO = \begin{cases} 1 - 4(PMO - 0.5)^2 & 0 \leq PMO \leq 0.5 \\ 1 & 0.5 < PMO \leq 1 \end{cases} \quad (21)$$

$$PMO = \begin{cases} 2PMO^2 & 0 \leq PMO \leq 0.5 \\ 1 - 2(1 - PMO)^2 & 0.5 < PMO \leq 1 \end{cases} \quad (22)$$

Figure 4.8 shows the effect of the above operations. The major advantage of a PMO image after median filtering (Figure 4.8(e)) is that without much change to the original intensity distribution range, the local contrast between foreground and background is increased and the texture of the image becomes smoother and clearer. Comparing Figures 4.8(a) and 4.8(e), we can see that the granular appearance inherent in ultrasound imaging is significantly reduced and the lesion boundary becomes clearer. Further contrast enhancement (Figure 4.8(f)) provides a better distinction between lesion and background for final segmentation. The average time cost of the obtaining the enhanced PMO image is 3.49 seconds.

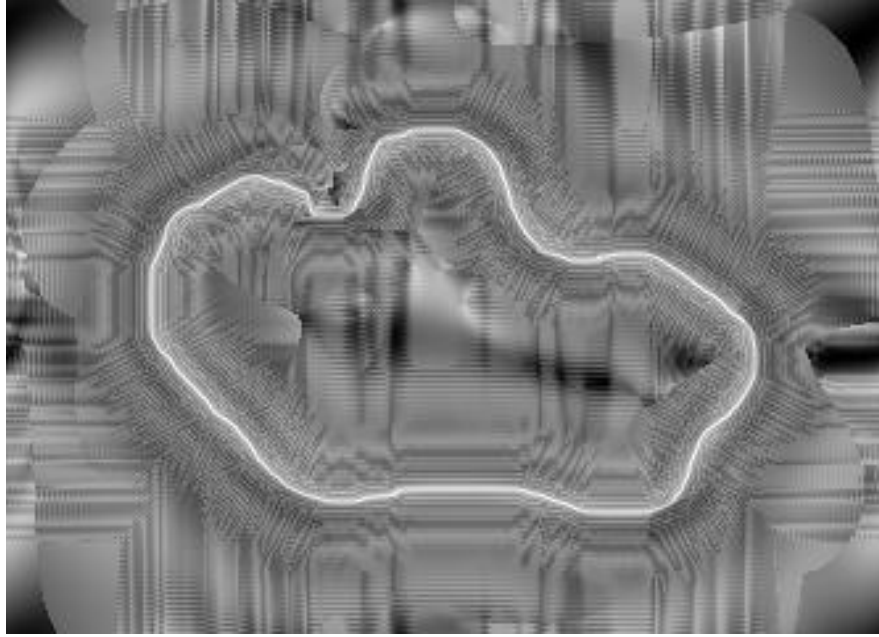


(a)



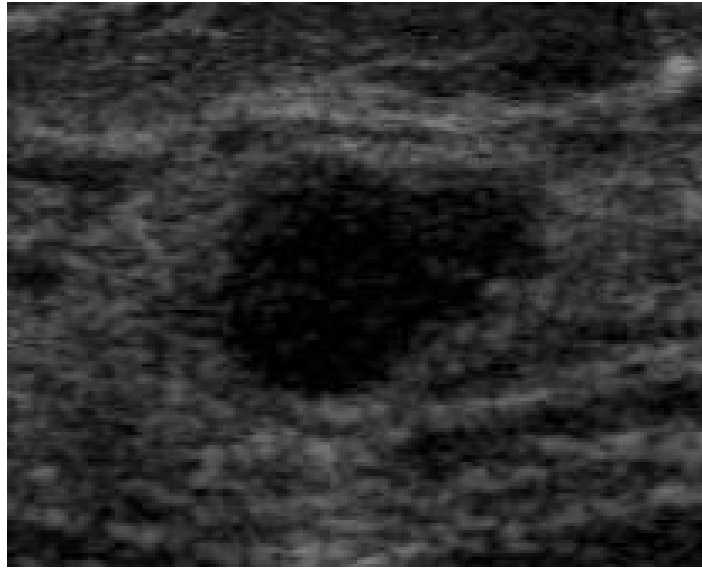
(b)

Figure 4.7. (a) The original image. (b) Phase summation feature image obtained by Eq. (18). (c) PMO feature image obtained by Eq. (19). (Continued on next page.)

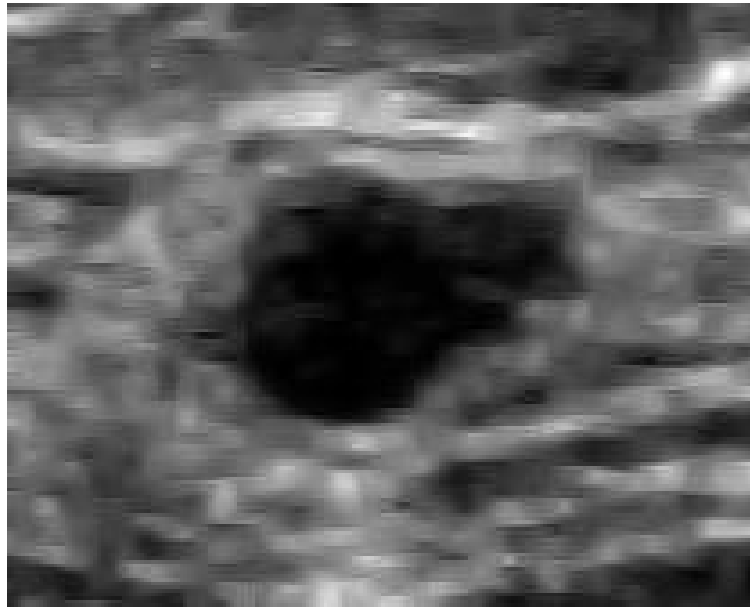


(c)

Figure 4.7. Cont. (a) The original image. (b) Phase summation feature image obtained by Eq. (18). (c) PMO feature image obtained by Eq. (19).



(a)

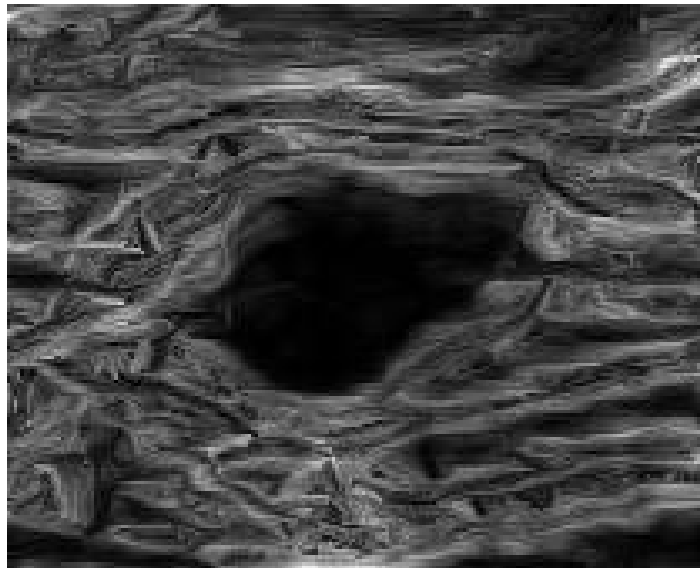


(b)

Figure 4.8. (a) ROI. (b) De-speckled image by the method in [58]. (c) PMO feature image. (d) PMO feature image after multiplying by the de-speckled image in (b). (e) PMO feature image after median filtering. (f) Enhanced PMO image after applying Eqs. (21) and (22). (Continued on next page.)

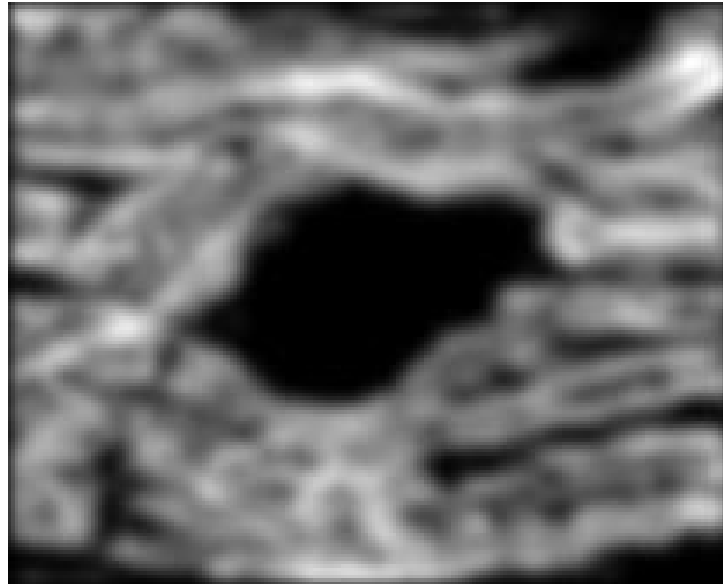


(c)



(d)

Figure 4.8. Cont. (a) ROI. (b) De-speckled image by the method in [58]. (c) PMO feature image. (d) PMO feature image after multiplying by the de-speckled image in (b). (e) PMO feature image after median filtering. (f) Enhanced PMO image after applying Eqs. (21) and (22). (Continued on next page.)



(e)



(f)

Figure 4.8. Cont. (a) ROI. (b) De-speckled image by the method in [58]. (c) PMO feature image. (d) PMO feature image after multiplying by the de-speckled image in (b). (e) PMO feature image after median filtering. (f) Enhanced PMO image after applying Eqs. (21) and (22).

CHAPTER 5

LESION DETECTION BY NEUTROSOPHIC L-MEANS

In this section, a neutrosophic l -means (NLM) clustering method is proposed. NLM is based on neutrosophy and fuzzy c-means to group pixels into a lesion region and background.

5.1 Fuzzy C-Means

The fuzzy c-means (FCM) is a soft clustering method wherein a datum is allowed to belong to two or more clusters. The algorithm was firstly developed by Dunn in 1973 [64] and improved by Bezdek in 1981 [65]. FCM is frequently used as clustering method in pattern recognition. It is based on the minimization of the following objective function:

$$J_m = \sum_{i=1}^N \sum_{j=1}^C u_{ij}^m \|x_i - c_j\|^2, \quad 1 \leq m < \infty \quad (23)$$

where m is a real number greater than 1, u_{ij} is the membership of x_i in cluster j , x_i is the i th of d -dimensional measured data, c_j is the d -dimensional center of the cluster, and $\|\cdot\|$ is any norm expressing the similarity between the data and the center.

Fuzzy partitioning is carried out through iterative optimization of the objective function above, with the update of membership u_{ij} and the cluster center c_j by:

$$u_{ij} = \frac{1}{\sum_{k=1}^c \left(\frac{\|x_i - c_j\|}{\|x_i - c_k\|} \right)^{\frac{2}{m-1}}} \quad (24)$$

$$c_j = \frac{\sum_{i=1}^N u_{ij}^m \cdot x_i}{\sum_{i=1}^N u_{ij}^m} \quad (25)$$

This iteration will stop when:

$$\max_{ij} \left\{ \left| u_{ij}^{(k+1)} - u_{ij}^k \right| \right\} < \varepsilon \quad (26)$$

where ε is a predefined termination criterion between 0 and 1, and k is the iteration step.

This procedure converges to a local minimum or a saddle point of J_m .

The algorithm is composed of the following steps:

Step 1: Initialize $U=[u_{ij}]$ matrix as $U^{(0)}$.

Step 2: At k -step: calculate the centers vector $C^{(k)}=[c_j]$ with $U^{(k)}$:

$$c_j = \frac{\sum_{i=1}^N u_{ij}^m \cdot x_i}{\sum_{i=1}^N u_{ij}^m} \quad (27)$$

Step 3: Update $U^{(k+1)}$:

$$u_{ij} = \frac{1}{\sum_{k=1}^C \left(\frac{\|x_i - c_j\|}{\|x_i - c_k\|} \right)^{\frac{2}{m-1}}} \quad (28)$$

Step 4: if $\|U^{(K+1)} - U^{(k)}\| < \varepsilon$, then STOP; otherwise, return to step 2.

5.2 Neutrosophy

Neutrosophy is a new branch of philosophy that studies the origin, nature, and scope of neutralities, as well as their interactions with different ideational spectra [66, 67]. It is the basis of neutrosophic logic, a branch of philosophy that generalizes fuzzy logic, and

deals with paradoxes, contradictions, antitheses, antinomies. The word neutrosophy, taken from the Latin ‘neuter’ – neutral, Greek ‘sophia’ – skill/wisdom was introduced by Smarandache in 1980 [66, 68]. It is a generalization of fuzzy logic based on the proposition that t true, i indeterminate, and f false. t, i, f are real values from the ranges T, I, F , with no restrictions on them. The following three examples help illustrate how neutrosophy is closer to human reasoning than other forms of logic [66].

1. The proposition "Tomorrow it will be raining" does not mean a fixed-valued components structure; this proposition may be, say, 40% true, 50% indeterminate, and 45% false at time t_1 ; but at time t_2 , it may change to 50% true, 49% indeterminate, and 30% false (based on new evidence, sources, etc.); and tomorrow at, say, time t_3 the same proposition may be 100% true, 0% indeterminate, and 0% false (if tomorrow it will indeed rain). This is the dynamics: the truth value for one given time may change for another given time.
2. The truth value of a proposition may change from one place to another place. For example, the proposition “It is raining” is 0% true, 0% indeterminate and 100% false in Albuquerque, New Mexico, but moving to Las Cruces, New Mexico the truth value can change, and it may be (1, 0, 0) or some other value.
3. The truth value depends/changes with respect to the observer (subjectivity is another parameter of the functions/operators T, I, F). For example: “John is smart” can be (0.35, 0.67, 0.60) according to his boss, but (0.80, 0.25, 0.10) according to himself, or (0.50, 0.20, 0.30) according to his secretary, etc.

Neutrosophic logic can solve some problems that cannot be solved by fuzzy logic [67]. For example, a case in which suspected breast cancer is diagnosed by two doctors. They both diagnose the case as malignant with 80% assurance. However, the two doctors may have different levels of background knowledge and experience. One is an expert, while the other is fresh in this field. The same assurance result should not have the same impact on the final diagnosis decision. There also exist a lot of other problems with indeterminacy, such as weather forecast, political elections, sporting events, etc. Fuzzy logic cannot handle indeterminate conditions in such matters very well [69]. Neutrosophy, on the other hand, introduces an indeterminacy set to deal with such conditions.

Definition 1 (Neutrosophic set) [66, 67]. Let U be a universe of disclosure, and $A \subset U$. An element x is denoted as $x(t, i, f)$, and belongs to A in the following way: it is $t\%$ true in the set, $i\%$ indeterminate, and $f\%$ false, where t varies in T , i varies in I , and f varies in F . The sets T , I , and F may be any real sub-unitary subsets: discrete or continuous; single-element, finite, or infinite; union or intersection of various subsets; etc. They may also overlap.

Figure 5.1 illustrates the relationship among a neutrosophic set and other sets. In a classical set, $I = \emptyset$, T and F have binary values 0 or 1, and $T + F = 1$. In a fuzzy set, $I = \emptyset$, T and F are real numbers $\in [0, 1]$, and $T + F = 1$. In a neutrosophic set, $I, T, F \in]0^-, 1^+[$.

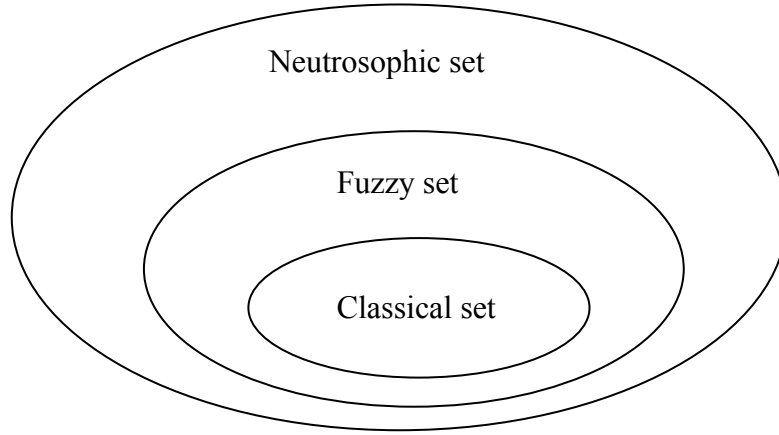


Figure 5.1. Relationships among a neutrosophic set and other sets.

5.3 Definitions of Neutrosophic Components for BUS Image Segmentation

When applying neutrosophy to solve a specific problem, one must map the problem into the neutrosophic domain by defining the neutrosophic components. In this proposal, the target is segmenting the lesion from the background. There are only two clusters: foreground (lesion) and background. For this application, the neutrosophic pixel and its neutrosophic components are defined as follows.

Definition 2 (Neutrosophic pixel) [67]. Let X be a universe of the pixels, and a foreground set $A \subset X$. A pixel p is noted as $p(t, i, f)$, and belongs to A in the following way: it is $t\%$ true in the foreground, $i\%$ indeterminate, and $f\%$ false, where t varies in T , i varies in I , and f varies in F . T , I , and F are real standard sets with the range $[0, 1]$.

Definition 3 (Neutrosophic components for a pixel). In an image, the three neutrosophic components T , I , and F for a pixel p at position (u, v) are defined as:

$$T(u, v) = 1 - G(u, v) \quad (29)$$

$$I(u, v) = BLUR(u, v) * (1 - EDGE(u, v)) \quad (30)$$

$$F(u, v) = 1 - T(u, v) \quad (31)$$

where

$$BLUR(u, v) = \begin{cases} 2(1 - T(u, v)) & T(u, v) \geq 0.5 \\ 2T(u, v) & T(u, v) < 0.5 \end{cases} \quad (32)$$

$$EDGE(u, v) = \begin{cases} 1 & \text{if } p \text{ is on the edge by sobel edge detector} \\ 0 & \text{if } p \text{ is not on the edge by sobel edge detector} \end{cases} \quad (33)$$

$G(u, v)$ is the intensity value normalized in $[0, 1]$. The motivation of the neutrosophic components definition is discussed below.

We use the intensity value normalized in $[0, 1]$ and subtracted by 1 as the T value. This is because a lesion is dark and the background is bright within the image. F value is the complement of T value. Although T and F are easily and simply defined, defining indeterminate set I is quite interesting and challenging. One should answer the following two questions: 1) what kind of pixels are hard to determine (with high indeterminacy) according to a specific task, and 2) how does one best deal with such pixels. In this paper, our target is separating pixels into two clusters: foreground and background. The foreground represents the lesion region and background includes all the pixels in the image except the lesion region. After preprocessing (de-speckle and contrast-enhancement), the image is composed of a dark lesion region, bright background, dark noise regions in the background, and some regions with intensity values somewhere in between the foreground and background. How we cluster the pixels with mediate intensities will greatly affect the segmentation accuracy. In order to assign high

indeterminacy to such pixels, we calculate a *BLUR* matrix by Eq. (32). The pixels with intensity values around 0.5 have a high indeterminacy value, and the pixels with intensity values near the extremes 0 or 1 have a low indeterminacy value. However, not all the pixels with mediate intensity should have a high indeterminacy value. If a pixel with mediate intensity lies on the lesion's edge, the pixel should not have a high indeterminate value. Otherwise, the edge will be blurred since we use neighborhood mean to replace a pixel with high indeterminacy. This is why we calculate an *EDGE* matrix using the Sobel edge detector, where the pixels on sharp edges are equal to 1 and other pixels are assigned 0. By multiplying *BLUR* and $(I - EDGE)$, only the pixels with mediate values and not on the edges have high indeterminate values.

The second question is how to deal with the pixels with high indeterminacy. Here, we use the neighborhood mean to replace the pixel with high indeterminate value:

$$G(u, v) = \frac{1}{w \times w} \sum_{s=i-w/2}^{i+w/2} \sum_{t=j-w/2}^{j+w/2} G(s, t) \quad (34)$$

where w is the window size and $G(u, v)$ is the intensity value. If we repeat the process, an indeterminate pixel inside a lesion will be gradually integrated into the lesion region, while an indeterminate pixel in the background will be gradually assimilated into the background. Notice that we only apply Eq. (34) for the pixels with high indeterminacy. The intensity value of pixels with low indeterminacy will not be changed. The threshold to distinguish high and low indeterminacy is discussed in the following section.

5.4 Neutrosophic L -Means (NLM)

Based on fuzzy c-means and the neutrosophic image defined above, a new clustering method for BUS image segmentation, called neutrosophic l -means (NLM) is proposed. NLM is composed of the following steps:

Step 1: Initialize membership matrix $U^{(k)} = [u_{ij}]$, $k = 0$. Here, i is the pixel index, j is the cluster index, and k is the iteration number.

Step 2: $k = k + 1$. At the k th iteration, calculate $T^{(k)}$, $I^{(k)}$, and $F^{(k)}$ for image $G^{(k)} (\mathcal{U} \times \mathcal{V})$ by using Eqs. (29) through (31), and transform $T^{(k)}$ and $I^{(k)}$ into vectors VT and VI .

Step 3: Calculate the center vector $L^{(k)} = [l_j]$ using $U^{(k)}$, VT , and VI .

$$l_j = \frac{\sum_{i=1}^N u_{ij}^m \cdot (1 - VI_i) \cdot VT_i}{\sum_{i=1}^N u_{ij}^m \cdot (1 - VI_i)} \quad (35)$$

where m is the membership parameter and N is the total number of pixels in the image. Here, the indeterminate degree VI is used to control a pixel's contribution to the cluster centers. If a pixel's indeterminate value is high, its contribution to all cluster centers is reduced. If a pixel's indeterminate value is low, its contribution to cluster centers is decided by its membership.

Step 4: Update $U^{(k+1)}$ by:

$$u_{ij} = \frac{1}{\sum_{d=1}^L \left(\frac{\|VT_i - l_j\|}{\|VT_i - l_d\|} \right)^{\frac{2}{m-1}}} \quad (36)$$

where L is the number of clusters.

Step 5: Update image $G^{(k+1)}$ by:

$$G^{(k+1)} = \begin{cases} G^{(k)} & \text{if } I^{(k)} < \lambda \\ G'^{(k)} & \text{if } I^{(k)} \geq \lambda \end{cases} \quad (37)$$

$$G'^{(k)}(u, v) = \frac{\sum_{s=u-w/2}^{u+w/2} \sum_{t=v-w/2}^{v+w/2} G^{(k)}(s, t)}{w^2} \quad (38)$$

where w is the size of the window, (u, v) is the location of the pixel centered the window, and λ is the indeterminacy threshold.

Step 6: If $\|U^{(k+1)} - U^{(k)}\| < \varepsilon$, stop; otherwise, go to step 2.

In this work, $L = 2$ since there are two clusters; $\varepsilon = 0.01$, $m = 2$, $w = 5$, and $\lambda = 0.1$ are determined by experiments. The output binary image is obtained by:

$$B(u, v) = \begin{cases} 1 & \text{If foreground membership } u_{i0} > \text{background membership } u_{i1} \\ 0 & \text{Otherwise} \end{cases} \quad (39)$$

Next, post-processing is conducted to remove false foreground regions. More than one connected component in binary image B implies that besides the real lesion region, there are false foreground regions. In Figure 5.2, region a is the lesion region which is the true foreground, while b, c, and d are the false foregrounds. Assuming there is only one lesion in each ROI, the way to find the real foreground is to choose the one that crosses the image center, because the lesion is always located at the center of the ROI when utilizing our ROI generation method. Therefore, only the connected component that crosses the image center is kept in the final output image. The average processing time of the NLM algorithm (include post-processing) is 6.51 seconds for one image.

The proposed method is able to recognize the tumor even when the output of NLM has a white hole inside the lesion area (e.g., Figure 5.2). The intensity value of a pixel with

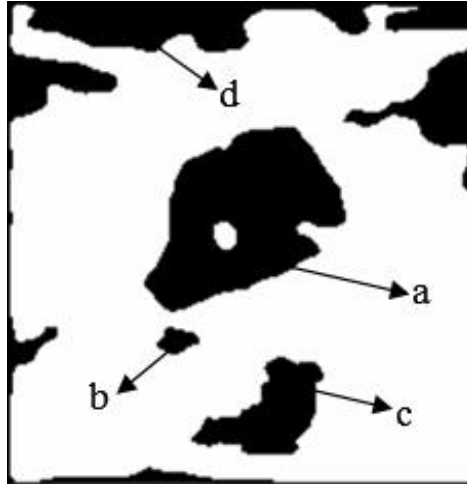


Figure 5.2 True foreground (a) and false foregrounds (b, c and d).

a high indeterminacy is replaced by the intensity mean of its neighborhood. Therefore, the boundary pixels of the bright area are gradually integrated into the dark area, and the bright area becomes smaller and smaller during the iterative process. However, if the center of the bright area is too bright, it will not completely disappear, and a white hole remains inside the lesion (Figure 5.2). The post-processing of the white hole depends on the task itself: if we just want to get the contours of the lesion, we can fill in the hole by a simple image operation (such as Matlab function '*imfill*'); if we want to keep the inhomogeneous information inside the lesion, which might be a useful feature to detect cancer, we can leave the hole unchanged. No matter which we prefer, the lesion is always recognized as a single lesion. In this work, all the holes inside the lesions are filled by morphological operations.

CHAPTER 6

EXPERIMENTAL RESULTS

To validate the proposed method, we compared it with other segmentation methods. The best way to make a fairly comparison among segmentation methods is to use a benchmark and evaluate the methods by a commonly accepted criterion. Unfortunately, very little published research in medical image segmentation field conducts a fair comparison with other methods. Without peer comparison, it is hard to claim how good a method is, even if it can achieve a promising performance by using its own database. In this section, we overcome this obstacle by conducting comparisons using a common database. We also evaluate the results statistically using multiple metrics (7 metrics are used here), which measure the segmentation performance comprehensively from different aspects.

6.1 Database

The database is composed of 60 BUS images: 29 cases are benign, 31 cases are malignant as confirmed by pathology. The images were collected by the doctors of the Second Affiliated Hospital of Harbin Medical University (Harbin, China), using a VIVID 7 (GE, Horten, Norway) with a 5-14 MHz linear probe. Informed consent to the protocol was obtained from all patients in the study. The average size of the images is 374×472 pixels. The size of the lesions ranges from 0.8 to 6.5 cm, and average size is 1.8 cm. Every lesion is manually outlined by an experienced radiologist. The manual delineations serve as the reference standard.

6.2 Evaluation Metrics

6.2.1 Area Error Metrics

Area error metrics can evaluate how much of the lesion region is correctly covered by the generated lesion region and how much is wrongly covered. The true positive (TP) area ratio, the false positive (FP) area ratio, the false negative (FN) area ratio [21] and the similarity (SI) [28] are calculated:

$$\text{TP Area Ratio} = \frac{|A_m \cap A_a|}{|A_m|} \quad (40)$$

$$\text{FP Area Ratio} = \frac{|A_m \cup A_a - A_m|}{|A_m|} \quad (41)$$

$$\text{FN Area Ratio} = 1 - \text{TP Area Ratio} = \frac{|A_m \cup A_a - A_a|}{|A_m|} \quad (42)$$

$$\text{SI} = \frac{|A_m \cap A_a|}{|A_m \cup A_a|} \quad (43)$$

A_a is the pixel set of the automatically generated lesion region by the proposed method, and A_m is the pixel set of the manually outlined lesion region by the radiologist. Figure 6.1 shows the areas corresponding to TP, FP, and FN, respectively. SI measures how much the computer generated lesion region is similar to the radiologist's delineation, which is an overall performance evaluation. Mathematically, if TP area ratio is given, there is no need to list the FN area ratio since $\text{FN} = 1 - \text{TP}$.

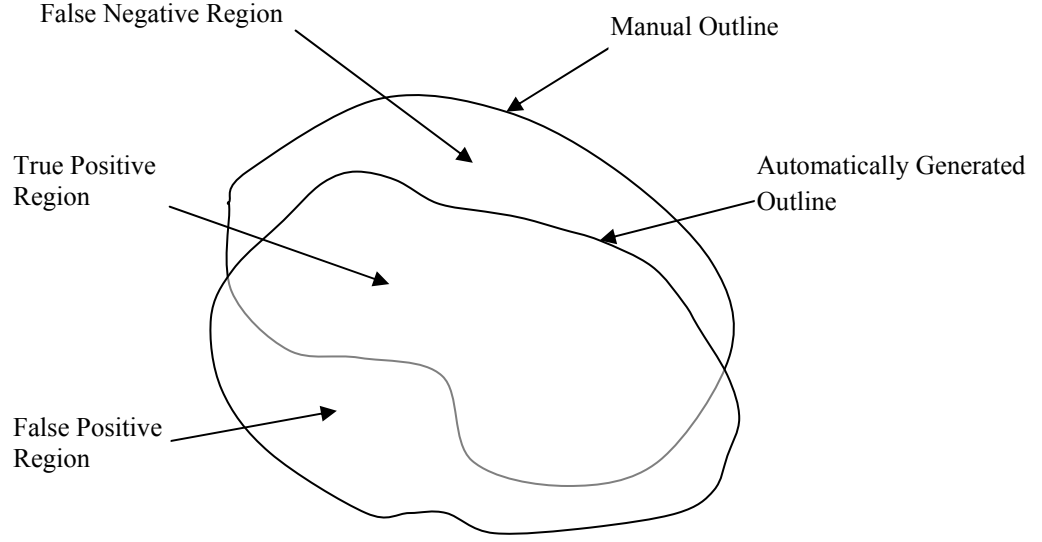


Figure 6.1. Areas corresponding to TP, FP, and FN regions.

6.2.2 Boundary Error Metrics

We use two boundary error metrics to analyze the difference between the contours generated by the proposed method and the contours marked by the radiologist. The two error metrics are Hausdorff distance (HD) and mean absolute distance (MD) [21]. We denote the manually delineated boundary as $Q = \{q_1, q_2, \dots, q_\nu\}$ and the computer segmented result as $P = \{p_1, p_2, \dots, p_\mu\}$, and each element of Q or P is a point on the corresponding contour. We find the distances of every point in P to all points in Q , and define the shortest distance of p_j to contour Q as:

$$\begin{aligned} \forall p_j \in P, j = 1, \dots, \mu, \text{ we find} \\ d(p_j, Q) = \min_w \|p_j - q_w\|, w = 1, \dots, \nu \end{aligned} \quad (44)$$

where $\|\cdot\|$ is 2D Euclidean distance. HD and MD are defined as:

$$HD = \max_j d(p_j, Q), j = 1, \dots, \mu \quad (45)$$

$$MD = \frac{\sum_{j=1}^{\mu} d(p_j, Q)}{\mu} \quad (46)$$

where γ and μ are the numbers of boundary pixels on contours Q and P , respectively. HD measures the worst possible disagreement between two contours while the MD measures the disagreement averaged over the two boundaries. The corresponding normalized errors Norm.HD and Norm.MD [21] are computed by:

$$\text{Norm.HD} = \frac{HD}{\gamma}, \text{ Norm.MD} = \frac{MD}{\gamma} \quad (47)$$

6.3 Comparison of NLM and Fuzzy C-Means

First, we compare NLM with FCM using the same database. Every preprocessing step is carried out exactly the same before applying NLM or FCM. Additionally, the same post-processing operations of removing false foreground and noisy regions are applied for both NLM and FCM. Figure 6.2(a) is the original image. Figure 6.2(b) is the enhanced PMO image. Figures 6.2(c) through (d) are the outputs of FCM and NLM, respectively. Figure 6.2(e) is the radiologist's manual delineation. Figure 6.3 shows another example. Table 6.1 provides a statistical analysis of the two methods.



(a)

Figure 6.2. (a) ROI automatically generated from original image. (b) Manually delineation by radiologist. (c) Enhanced PMO image. (d) Output of FCM. (e) Output of FCM after post-processing. (f) Output of NLM. (g) Output of NLM after post-processing. (Continued on next page.)

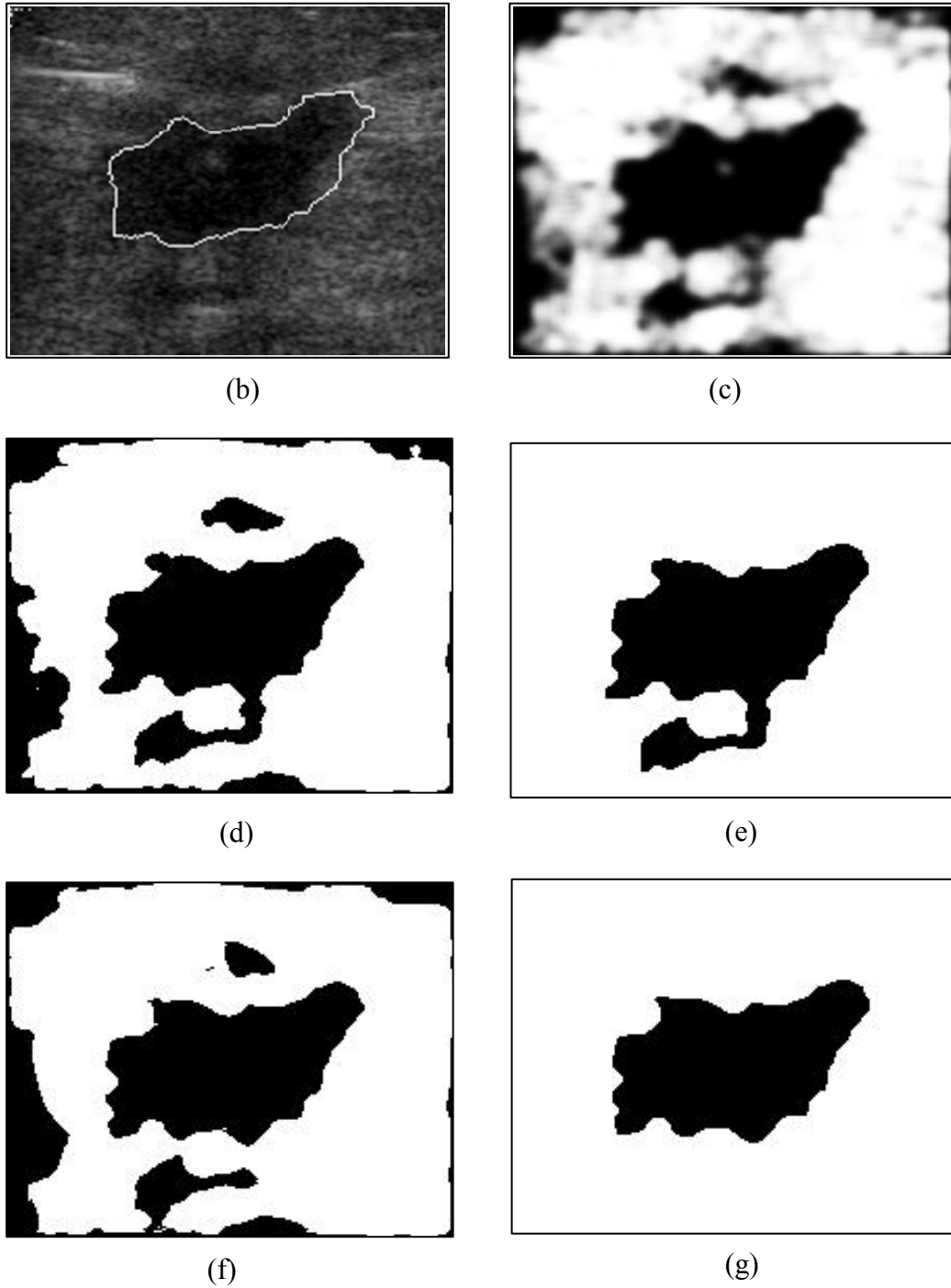
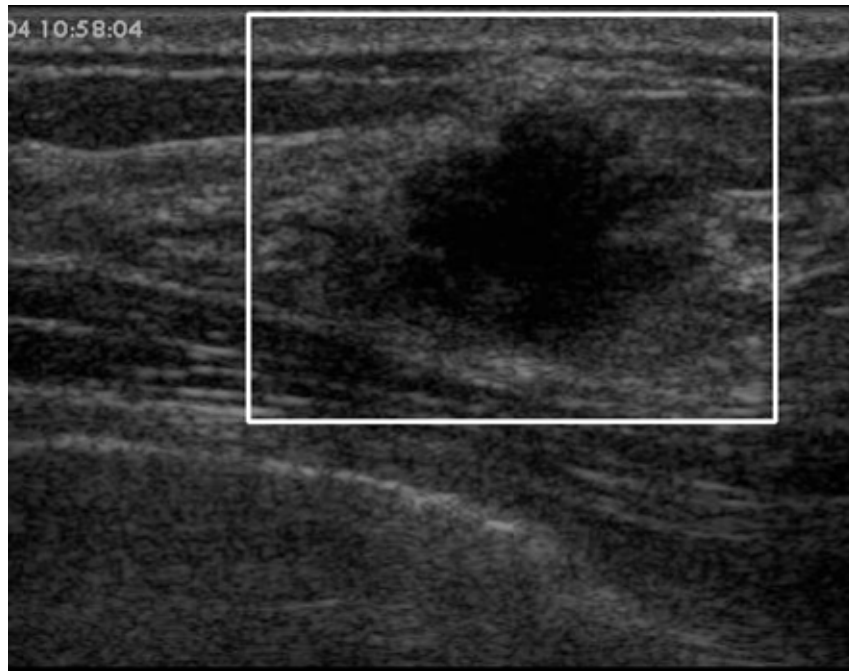


Figure 6.2. Cont. (a) ROI automatically generated from original image. (b) Manually delineation by radiologist. (c) Enhanced PMO image. (d) Output of FCM. (e) Output of FCM after post-processing. (f) Output of NLM. (g) Output of NLM after post-processing.



(a)

Figure 6.3. (a) ROI automatically generated from original image. (b) Manually delineation by radiologist. (c) Enhanced PMO image. (d) Output of FCM. (e) Output of FCM after post-processing. (f) Output of NLM. (g) Output of NLM after post-processing. (Continued on next page.)

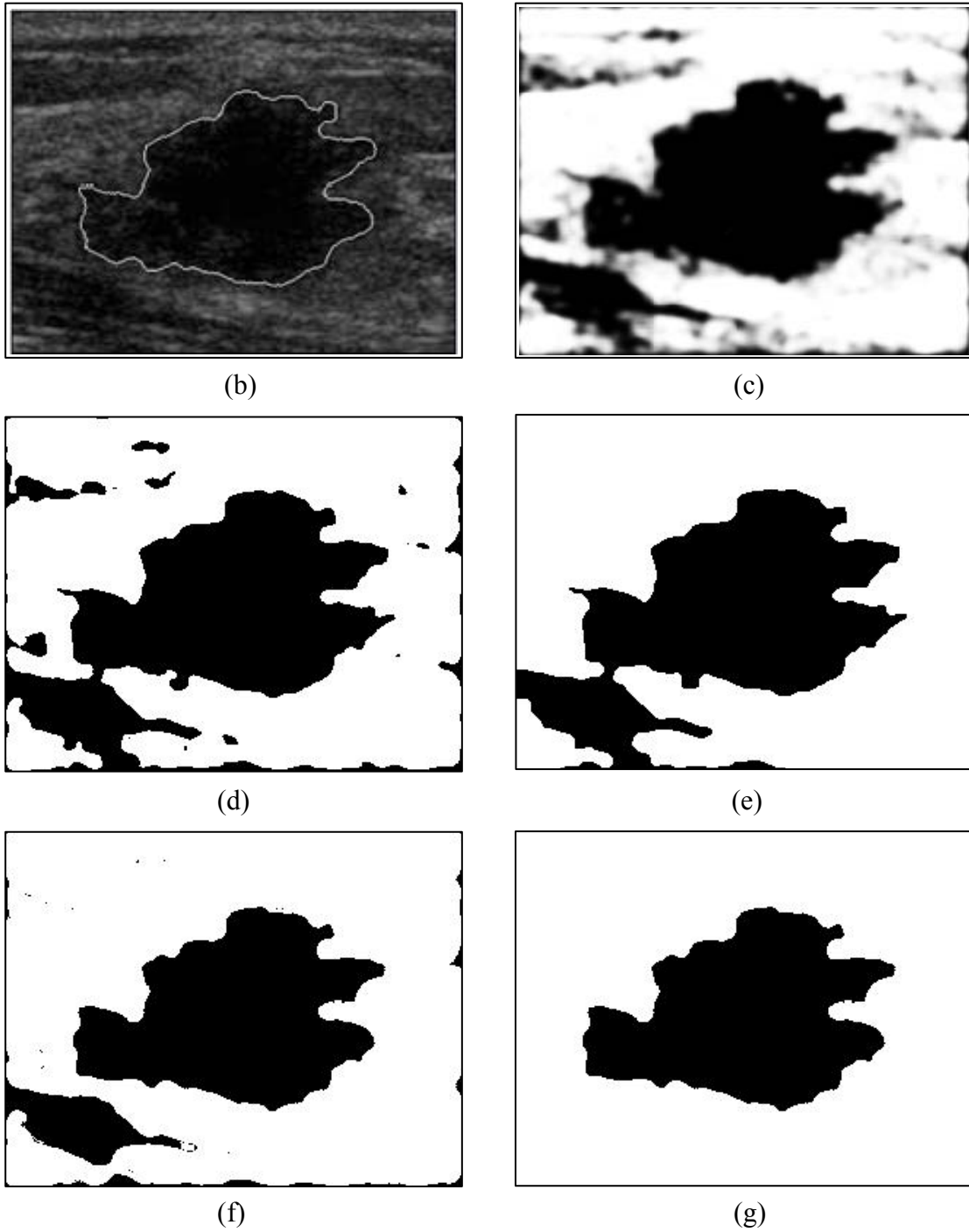


Figure 6.3. Cont. (a) ROI automatically generated from original image. (b) Manually delineation by radiologist. (c) Enhanced PMO image. (d) Output of FCM. (e) Output of FCM after post-processing. (f) Output of NLM. (g) Output of NLM after post-processing.

The major advantage of NLM over FCM is that NLM can deal with indeterminate intensity regions effectively and accurately. As Figure 6.2 shows, based on the neighborhood information, NLM incorporates the indeterminate regions into background. But FCM misclassifies the indeterminate regions into foreground, since it uses only the distance to calculate the cluster centers (fuzzy membership is based on distance, too), without considering the indeterminate degree. Another advantage of NLM is that it can smooth the complex background; therefore, it can prevent the lesion region from connecting with the false foregrounds. Figure 6.3 gives such an example. The lesion region obtained by NLM (Figure 6.3 (f)) is not connected with any dark region in the background. Therefore, after the simple post-processing, the lesion boundary obtained by NLM is quite clear and accurate (Figure 6.3 (g)). On the contrary, the output of FCM (Figure 6.3(d)) has many false foreground and noisy regions. Although we apply the same post-processing operation to FCM, the result still mis-connects with one of the false foreground regions (Figure 6.3 (e)). Statistically, 25% of the images in the database mis-connect with false foregrounds by using FCM. Besides the above two major advantages, NLM finds more accurate lesion boundaries than FCM. This can be seen from the statistical analysis in Table 6.1.

Table 6.1. Comparison of NLM and FCM.

Methods	Area error metrics			Boundary error metrics				Average time/case
	TP(%)	FP(%)	SI(%)	Avg.HD	Avg.MD	Norm.HD	Norm.MD	
FCM	89.83	8.68	83.49	28.76	5.63	5.64	1.20	3.92s
NLM	94.36	8.08	87.39	16.63	3.48	3.17	0.70	6.51s

As Table 6.1 shows, NLM outperforms FCM in all the accuracy metrics. The higher TP rate (improved from 89.83% to 94.36%) indicates that NLM covers more of the lesion region than the other two methods. The lower FP rate (decreased from 9.03% to 8.08%) indicates less mis-coverage of the non-lesion regions. SI is an overall evaluation of the similarity between the two regions, and an improvement from 83.49% to 87.39% is quite remarkable. The better performance of NLM is proven by the boundary error metrics, too. Here, we want to emphasize that the average Hausdorff distance (measure the worst point-distance between two contours) is reduced from 28.76 to 16.63 pixels, and the average mean distance is reduced from 5.63 to 3.48 pixels, which indicate that the contours generated by NLM are much closer to the manual delineations. The time cost of FCM (3.92 seconds) is faster than that of NLM (6.51 seconds). Although NLM takes about 3 seconds longer than FCM for an average case, NLM can achieve much better accuracy and its processing speed is quite acceptable for clinical applications. The longer processing time is spent on computation of the neutrosophic components for each pixel; however, it makes the clustering process more precise.

6.4 Comparison of the Proposed Method with Other BUS Segmentation Methods

In this section, we compare the proposed method with three other automatic segmentation methods for BUS images. The first one is a highly cited BUS segmentation method based on active contour [21], that uses low-level texture information to find the points on a boundary and employs an active contour model to detect the final lesion boundary; the second is a level-set-based method [28], combining both global statistical

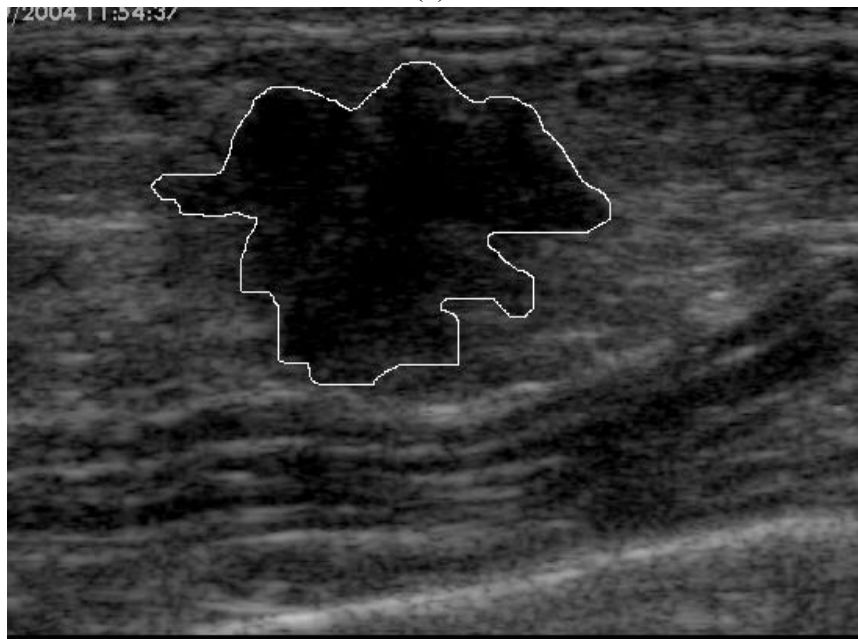
information and local edge information; the third is a watershed-based segmentation method that applies neutrosophy as proposed by Zhang [70].

Figure 6.4 shows the segmentation results of the four methods. Figure 6.4(a) is the original image. Figure 6.4(b) is the manual delineation by a radiologist, which serves as the reference standard. Figures 6.4 (c) through (f) are the segmentation results of the method in [21], the method in [28], the method in [70], and the proposed method, respectively. The lesion boundary detected by the proposed method is much closer to the radiologist's manual delineation and more reasonable than that of the other three methods.

The statistical analyses of the performances of the four methods are conducted by using the same database. Tables 6.2 and 6.3 list the accuracies and time complexities of the four methods. Compared with the other three methods, the proposed method achieves the best TP, FP, and SI rates. Greatly reduced Hausdorff distance (HD) and other boundary error metrics also show the contour generated by the proposed method is closer to the ground truth than that of the other three methods on average. Time complexity of the proposed method is comparable with that of the active contour method in [21] and much more efficient than that of the level-set based method in [28]. The most efficient is the watershed based method [70] (only 5 seconds); however, its accuracy is low. All in all, the proposed method achieves the best accuracy while keeping a reasonable processing time, when compared with the other three methods.

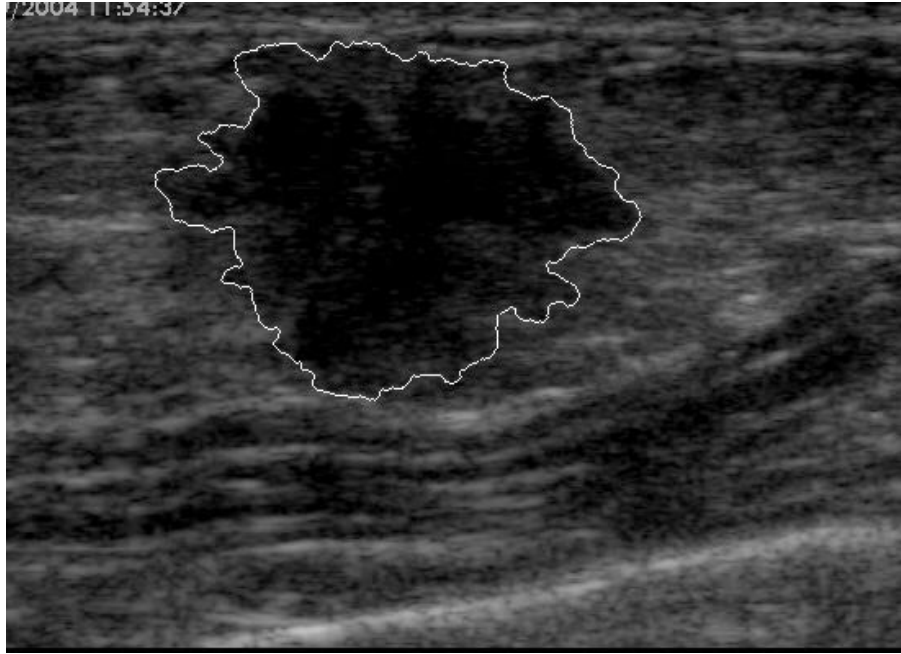


(a)

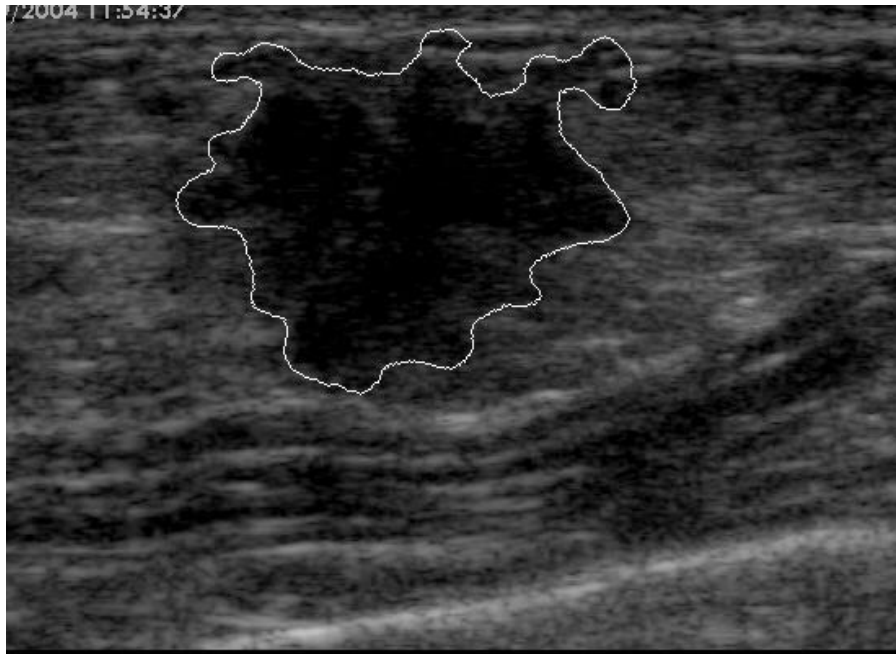


(b)

Figure 6.4. (a) The original image. (b) Manual delineation by radiologist. (c) Output of the method in [21]. (d) Output of the method in [28]. (e) Output of the method in [70]. (f) Output of the proposed method. (Continued on the next page.)

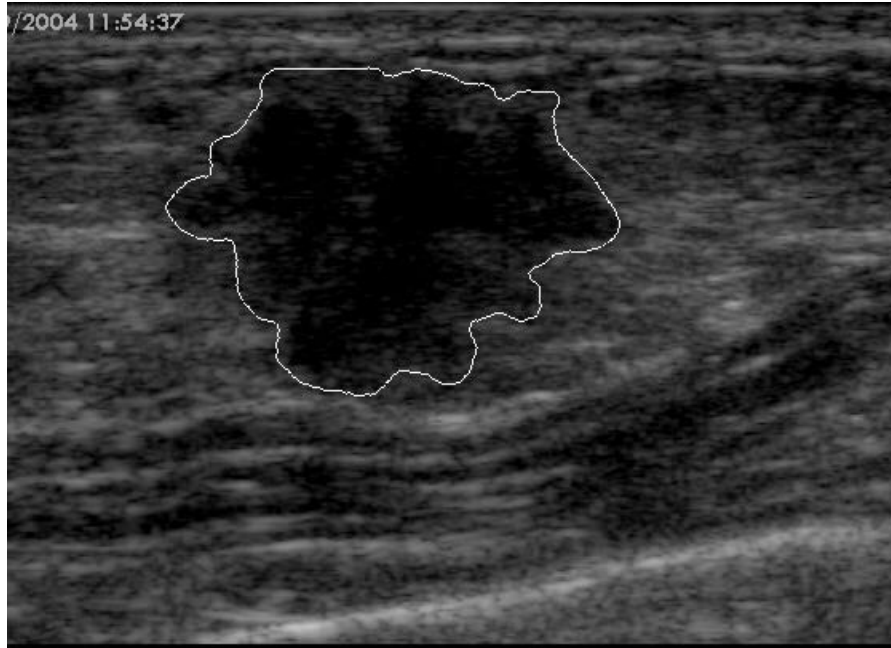


(c)

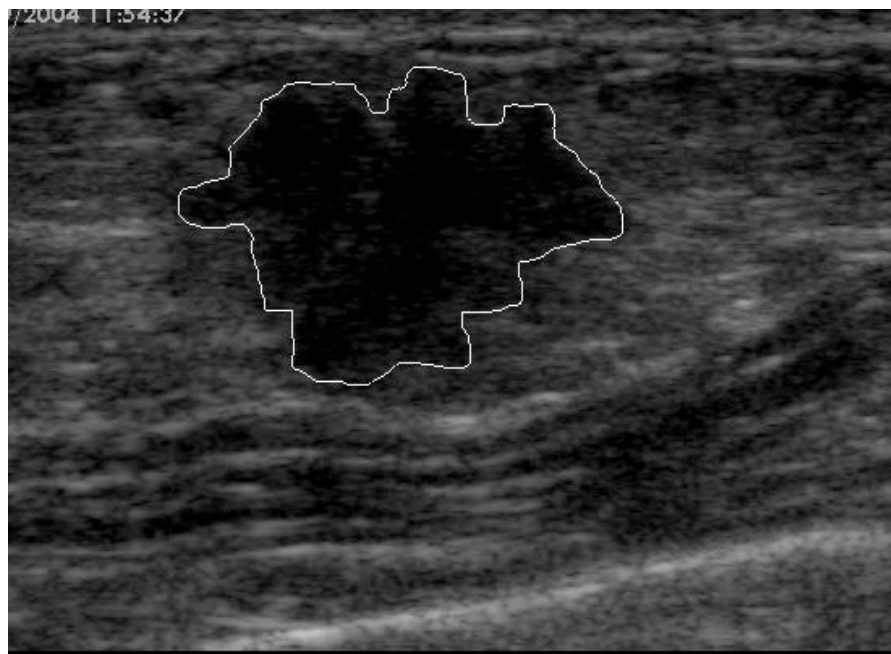


(d)

Figure 6.4. Cont. (a) The original image. (b) Manual delineation by radiologist. (c) Output of the method in [21]. (d) Output of the method in [28]. (e) Output of the method in [70]. (f) Output of the proposed method. (Continued on the next page.)



(e)



(f)

Figure 6.4. Cont. (a) The original image. (b) Manual delineation by radiologist. (c) Output of the method in [21]. (d) Output of the method in [28]. (e) Output of the method in [70]. (f) Output of the proposed method.

Table 6.2. Comparison of Accuracy of the Active Contour Method [21], Level-Set Method [28], Watershed Method [70], and the Proposed Method.

Methods	Area error metrics			Boundary error metrics			
	TP(%)	FP(%)	SI(%)	Avg.HD	Avg.MD	Norm.HD	Norm.MD
Method in [21]	88.50	9.68	80.51	19.96	5.13	4.03	1.09
Method in [28]	92.98	9.03	85.98	23.52	4.39	4.75	0.93
Method in [70]	89.49	19.25	75.54	22.97	7.46	4.52	1.50
Proposed method	94.36	8.08	87.39	16.63	3.48	3.17	0.70

Table 6.3. Comparison of Time Complexity of the Active Contour Method [21], Level-Set Method [28], Watershed Method [70], and the Proposed Method.

Methods	Average time/case
Method in [21]	21.90s
Method in [28]	60.06s
Method in [70]	5.08s
Proposed method	20.43s

6.5 Sensitivity Analysis

A method is robust if its performance is almost insensitive to variation of the parameters [71]. We conducted sensitivity analysis by varying the parameters used in the proposed method. The tunable parameters are m (for membership calculation), w (for the size of window), and λ (for the threshold of indeterminate value).

6.5.1 Effect of Tuning Membership Parameter m

The parameter m is used to calculate membership in Eq. (36). We varied m and computed the standard deviations (std) of the area error and boundary error metrics. As Table 6.4 shows, none of the area error metrics' stds exceed 0.2%, and all the boundary error metrics' stds are under 0.4 pixel, i.e., the proposed method is quite robust to parameter m .

Table 6.4 Performance and Standard Deviation for Different Values of m .

m	Area error metrics			Boundary error metrics			
	TP(%)	FP(%)	SI(%)	Avg.HD	Avg.MD	Norm.HD	Norm.MD
2	94.36	8.08	87.39	16.63	3.48	3.17	0.70
3	94.07	8.24	86.98	17.42	3.63	3.33	0.74
4	94.40	8.35	87.22	16.99	3.54	3.25	0.72
5	94.39	8.36	87.20	17.28	3.56	3.30	0.72
Std	0.16	0.13	0.17	0.35	0.06	0.07	0.02

6.5.2 Effect of Tuning Window Size w

The parameter w represents the window size used in NLM algorithm step 5. We varied w to calculate the stds. The small stds for all the evaluation metrics shown in Table 6.5 prove that the proposed method is robust to window size.

Table 6.5 Performance and Standard Deviation for Different Values of w .

w	Area error metrics			Boundary error metrics			
	TP(%)	FP(%)	SI(%)	Avg.HD	Avg.MD	Norm.HD	Norm.MD
3	94.38	8.40	87.17	17.47	3.58	3.35	0.73
5	94.36	8.08	87.39	16.63	3.48	3.17	0.70
7	94.06	8.65	86.74	17.72	3.76	3.35	0.75
9	94.03	9.84	85.83	18.32	4.01	3.49	0.81
Std	0.19	0.77	0.69	0.70	0.23	0.13	0.05

6.5.3 Effect of Tuning Threshold λ

We tune indeterminacy threshold λ and record the evaluation results in Table 6.6. The small stds for all the evaluation metrics soundly demonstrate that the proposed method is robust to parameter λ .

Table 6.6 Performance and Standard Deviation for Different Values of λ .

λ	Area error metrics			Boundary error metrics			
	TP(%)	FP(%)	SI(%)	Avg.HD	Avg.MD	Norm.HD	Norm.MD
0.1	94.36	8.08	87.39	16.63	3.48	3.17	0.70
0.2	94.38	8.27	87.26	17.00	3.52	3.25	0.72
0.3	94.45	8.32	87.29	17.32	3.54	3.31	0.72
Std	0.05	0.13	0.07	0.35	0.03	0.07	0.01

6.6 Limitations of the Proposed Method

The proposed method can deal with normal shadowing effect but fails with the images having strong posterior shadows. Strong posterior shadows include the cases that the intensity values of lesion and shadow are quite close and they are tightly connected. These shadowed regions can lead to false-positives (Figure 6.5). Also, the case with multiple lesions in one image is not included in this study (Figure 6.6). These problems will be the focus of future research.

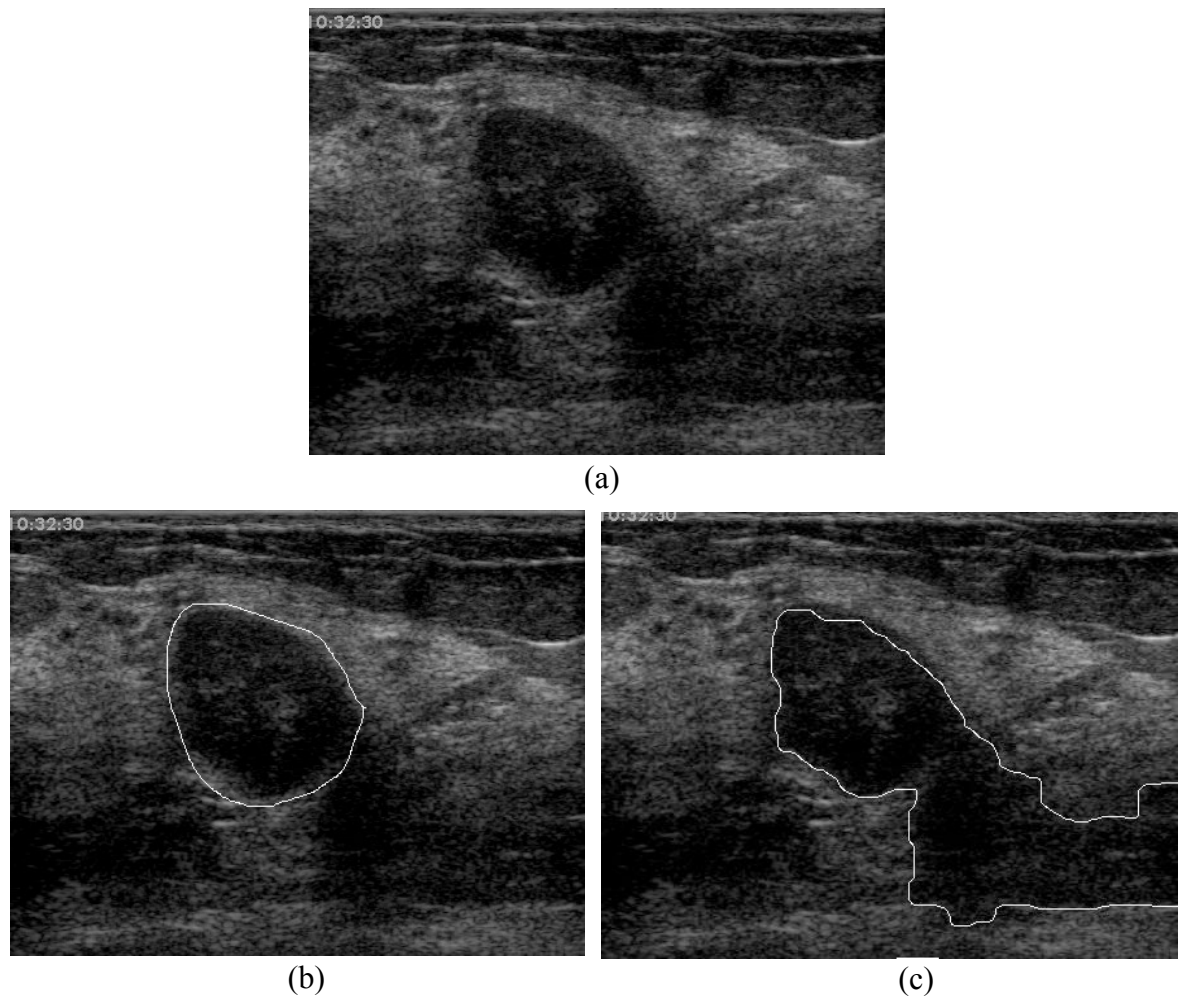
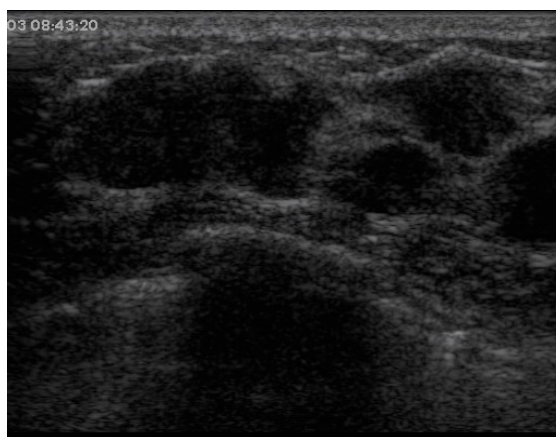
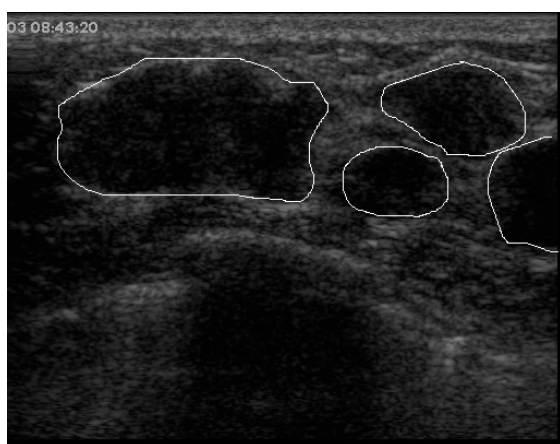


Figure 6.5. (a) A case with posterior shadowing. (b) Manual delineation by radiologist.

(c) Output of the proposed method.



(a)



(b)



(c)

Figure 6.6. (a) A case with multiple lesions. (b) Manual delineation by radiologist.

(c) Output of the proposed method.

CHAPTER 7

CONCLUSIONS AND FUTURE DIRECTIONS FOR RESEARCH

In this dissertation, we study lesion boundary detection for breast ultrasound images and propose a novel lesion segmentation method. The proposed segmentation method is composed of several steps: automatic ROI generation, speckle reduction, contrast enhancement, and neutrosophic *l*-means clustering (NLM). Automatic ROI (region of interest) generation facilitates the full automation of the segmentation method and speeds up the segmentation process. Complicated background is removed from the image; hence, the method focuses on the lesion area rather than the entire image, and segmentation accuracy is improved. Two different speckle reduction methods are studied, and one is used in this work as a preprocessing step. A novel local phase feature PMO is proposed and utilized to enhance the contrast and quality for the BUS images. In the neutrosophic *l*-means clustering, the neutrosophy, a new branch of philosophy, is applied to image segmentation. Through a comparison with traditional fuzzy c-means, the positive effect of applying neutrosophy is demonstrated. To evaluate the whole segmentation method proposed in this work, a quantitative analysis of both accuracy and efficiency are conducted on the database composed of 60 BUS images. Comparison with other BUS image segmentation methods using the same database proves the superiority of the proposed method. Finally, sensitivity analysis shows the robustness of the newly proposed segmentation method.

The advantages of the proposed method can be summarized as:

1. It is completely automatic.

2. It finds the accurate lesion boundaries even in complicated and low-contrast BUS images.
3. In accuracy, it outperforms the fuzzy c-means clustering as well as three other BUS segmentation methods. Experiments are carried out using a common database and the performance is evaluated by a set of comprehensive criteria.
4. The analysis time of the proposed method is about 20 seconds for each case, which is more efficient than the active-contour-based method and the level-set-based method. The watershed-based-method is the fastest, but unfortunately it trades speed for accuracy, with its accuracy rate being the lowest among the methods studied in this work.
5. The proposed method is quite robust.

One limitation of the proposed method is that it sometimes fails in cases containing large posterior shadowing areas connected with the lesion. A second limitation of the proposed method is that it can detect the contours of only one lesion per image. These problems will be addressed in future research. Another future direction is to use this method for other applications, such as echocardiography, prostate ultrasound, etc. Since this method is based on the characteristics of ultrasound imaging, it should be easily adjusted for other ultrasound images. Future work also includes classifying the lesions into benign/malignant based on the features extracted from the segmentation results.

REFERENCES

1. Cheng, H.D., Shan, J., Ju, W., Guo, Y., and Zhang, L. Automated breast cancer detection and classification using ultrasound images: A survey. *Pattern Recognition* 43, 1 (2010), 299-317.
2. Jemal, A., Siegel, R., Xu, J., and Ward, E. Cancer statistics 2010. *CA Cancer J. for Clinicians* 60, (2010), 227-300.
3. Cheng, H.D., Shi, X.J., Min, R., Hu, L.M., Cai, X.P., and Du, H.N. Approaches for automated detection and classification of masses in mammograms. *Pattern Recognition* 39, 4 (2006), 646-668.
4. Cheng, H.D., Cai, X., Chen, X., Hu, L., and Lou, X. Computer-aided detection and classification of microcalcifications in mammograms: A survey. *Pattern Recognition* 36, 12 (2003), 2967-2991.
5. Jesneck, J., Lo, J., and Baker, J. Breast mass lesions: Computer-aided diagnosis models with mammographic and sonographic descriptors. *Radiology* 244, 2 (2007), 390-398.
6. Shankar, P.M., Piccoli, C.W., Reid, J.M., Forsberg, F., and Goldberg, B.B. Application of the compound probability density function for characterization of breast masses in ultrasound B scans. *Physics in Medicine & Biology* 50, 10 (2005), 2241-2248.
7. Taylor, K.J.W., Merritt, C., Piccoli, C., Schmidt, R., Rouse, G., Fornage, B., Rubin, E., Georgian-Smith, D., Winsberg, F., Goldberg, B., and Mendelson, E. Ultrasound as a complement to mammography and breast examination to

- characterize breast masses. *Ultrasound in Medicine & Biology* 28, 1 (2002), 19-26.
8. Zhi, H., Ou, B., Luo, B.-M., Feng, X., Wen, Y.-L., and Yang, H.-Y. Comparison of ultrasound elastography, mammography, and sonography in the diagnosis of solid breast lesions. *J. Ultrasound in Medicine* 26, 6 (2007), 807-815.
 9. Chang, R.-F., Wu, W.-J., Moon, W.K., and Chen, D.-R. Improvement in breast tumor discrimination by support vector machines and speckle-emphasis texture analysis. *Ultrasound in Medicine & Biology* 29, 5 (2003), 679-686.
 10. Sahiner, B., Chan, H.-P., Roubidoux, M.A., Hadjiiski, L.M., Helvie, M.A., Paramagul, C., Bailey, J., Nees, A.V., and Blane, C. Malignant and benign breast masses on 3D US volumetric images: Effect of computer-aided diagnosis on radiologist accuracy. *Radiology* 242, 3 (2007), 716-724.
 11. Chen, C.-M., Chou, Y.-H., Han, K.-C., Hung, G.-S., Tiu, C.-M., Chiou, H.-J., and Chiou, S.-Y. Breast lesions on sonograms: Computer-aided diagnosis with nearly setting-independent features and artificial neural networks. *Radiology* 226, 2 (2003), 504-514.
 12. Drukker, K., Giger, M.L., Horsch, K., Kupinski, M.A., Vyborny, C.J., and Mendelson, E.B. Computerized lesion detection on breast ultrasound. *Medical Physics* 29, 7 (2002), 1438-1446.
 13. Andr, M.P., Galperin, M., Olson, L.K., Richman, K., Payrovi, S., and Phan, P. Improving the accuracy of diagnostic breast ultrasound. *Acoustical Imaging* 26, (2002), 453-460.

14. Huang, Y.-L., Chen, D.-R., and Liu, Y.-K. Breast cancer diagnosis using image retrieval for different ultrasonic systems. In *International Conference on Image Processing*, 2004, 2957-2960.
15. Anderson, B., Shyyan, R., Eniu, A., Smith, R., and Yip, C. Breast cancer in limited-resource countries: An overview of the breast health global initiative 2005 guidelines. *Breast Journal* 12, 1 (2006), S3-15.
16. Hwang, K.-H., H., Lee, J.G., Kim, J.H., Lee, H.-J. Om, K.-S., Yoon, M., and Choe, W. Computer aided diagnosis (CAD) of breast mass on ultrasonography and scintimammography. In *Proceedings of 7th International Workshop on Enterprise Networking and Computing in Healthcare Industry*, 2005, 187-189.
17. American-College-of-Radiology, ACR standards 2000-2001. 2000: Reston, VA.
18. Noble, J.A. and Boukerroui, D. Ultrasound image segmentation: A survey. *IEEE Trans. on Medical Imaging* 25, 8 (2006), 987-1010.
19. Joo, S., Moon, W.K., and Kim, H.C. Computer-aided diagnosis of solid breast nodules on ultrasound with digital image processing and artificial neural network. In *26th Annual IEEE International Conference Proceedings on Engineering in Medicine and Biology Society*, 2004, 1397-13400.
20. Chen, D.-R., Chang, R.-F., and Huang, Y.-L. Computer-aided diagnosis applied to US of solid breast nodules by using neural networks. *Radiology* 213, 2 (1999), 407-412.

21. Madabhushi, A. and Metaxas, D.N. Combining low-, high-level and empirical domain knowledge for automated segmentation of ultrasonic breast lesions. *IEEE Trans. on Medical Imaging* 22, 2 (2003), 155-169.
22. Xiaohui, H., Bruce, C.J., Pislaru, C., and Greenleaf, J.F. Segmenting high-frequency intracardiac ultrasound images of myocardium into infarcted, ischemic, and normal regions. *IEEE Trans. on Medical Imaging* 20, 12 (2001), 1373-1383.
23. Joo, S., Yang, Y.S., Moon, W.K., and Kim, H.C. Computer-aided diagnosis of solid breast nodules: Use of an artificial neural network based on multiple sonographic features. *IEEE Trans. on Medical Imaging* 23, 10 (2004), 1292-1300.
24. Yeh, C.-K., Chen, Y.-S., Fan, W.-C., and Liao, Y.-Y. A disk expansion segmentation method for ultrasonic breast lesions. *Pattern Recognition* 42, 5 (2009), 596-606.
25. Horsch, K., Giger, M.L., Venta, L.A., and Vyborny, C.J. Computerized diagnosis of breast lesions on ultrasound. *Medical Physics* 29, 2 (2002), 157-164.
26. Horsch, K., Giger, M.L., Venta, L.A., and Vyborny, C.J. Automatic segmentation of breast lesions on ultrasound. *Medical Physics* 28, 8 (2001), 1652-1659.
27. Chang, R.F., Wu, W.J., Moon, W.K., and Chen, D.R. Automatic ultrasound segmentation and morphology based diagnosis of solid breast tumors. *Breast Cancer Research and Treatment* 89, 2 (2005), 179-185.
28. Liu, B., Cheng, H.D., Huang, J., Tian, J., Liu, J., and Tang, X., Automated segmentation of ultrasonic breast lesions using statistical texture classification and

- active contour based on probability distance. *Ultrasound in Medicine & Biology* 35, 8 (2009), 1309-1324.
29. Sarti, A., Corsi, C., Mazzini, E., and Lamberti, C. Maximum likelihood segmentation with Rayleigh distribution of ultrasound images. *Computers in Cardiology* 31 (2004), 329-332.
 30. Chang, R.-F., Wu, W.-J., Moon, W.K., Chen, W.-M., Lee, W., and Chen, D.-R. Segmentation of breast tumor in three-dimensional ultrasound images using three-dimensional discrete active contour model. *Ultrasound in Medicine & Biology* 29, 11 (2003), 1571-1581.
 31. Chen, D.-R., Chang, R.-F., Wu, W.-J., Moon, W.K., and Wu, W.-L. 3-D breast ultrasound segmentation using active contour model. *Ultrasound in Medicine & Biology* 29, 7 (2003), 1017-1026.
 32. Chang, R.F., Wu, W.J., Tseng, C., Chen, D.R., and Moon, W.K. 3-D snake for US in margin evaluation for malignant breast tumor excision using mammotome. *IEEE Trans. on Information Technology in Biomedicine* 7, 3 (2003), 197-201.
 33. Sahiner, B., Chan, H.-P., Roubidoux, M.A., Helvie, M.A., Hadjiiski, L.M., Ramachandran, A., Paramagul, C., LeCarpentier, G.L., Nees, A., and Blane, C. Computerized characterization of breast masses on three-dimensional ultrasound volumes. *Medical Physics* 31, 4 (2004), 744-754.
 34. Boukerroui, D., Baskurt, A., Noble, J.A., and Basset, O. Segmentation of ultrasound images--multiresolution 2D and 3D algorithm based on global and local statistics. *Pattern Recognition Letters* 24, 4-5 (2003), 779-790.

35. Xiao, G., Brady, M., Noble, J.A., and Zhang, Y. Segmentation of ultrasound B-mode images with intensity inhomogeneity correction. *IEEE Trans. on Medical Imaging* 21, 1 (2002), 48-57.
36. Cheng, H.D., Hu, L.M., Tian, J.W., and Sun, L., A novel Markov random field segmentation algorithm and its application to breast ultrasound image analysis. In *6th International Conference on Computer Vision, Pattern Recognition and Image Processing*, 2005, 644-647.
37. Boukerroui, D., Basset, O., Guérin, N., and Baskurt, A. Multiresolution texture based adaptive clustering algorithm for breast lesion segmentation. *European J. Ultrasound* 8, 2 (1998), 135-144.
38. Christopher, L.A., Delp, E.J., Meyer, C.R., and Carson, P.L. 3-D Bayesian ultrasound breast image segmentation using the EM/MPM algorithm. In *Proceedings of IEEE International Symposium on Biomedical Imaging*, 2002, 86-89.
39. Kotropoulos, C. and Pitas, I. Segmentation of ultrasonic images using support vector machines. *Pattern Recognition Letters* 24, 4-5 (2003), 715-727.
40. Zhan, Y. and Shen, D. Deformable segmentation of 3-D ultrasound prostate images using statistical texture matching method. *IEEE Trans. on Medical Imaging* 25, 3 (2006), 256-272.
41. Wu, H.-M. and Lu, H.H.-S. Iterative sliced inverse regression for segmentation of ultrasound and MR images. *Pattern Recognition* 40, 12 (2007), 3492-3502.

42. Dokur, Z. and Ölmez, T. Segmentation of ultrasound images by using a hybrid neural network. *Pattern Recognition Letters* 23, 14 (2002), 1825-1836.
43. Işcan, Z., Kurnaz, M.N., Dokur, Z., and Ölmez, T. Letter: Ultrasound image segmentation by using wavelet transform and self-organizing neural network. *Neural Information Processing - Letters and Reviews* 10, 8-9 (2006).
44. Huang, Y.-L. and Chen, D.-R. Watershed segmentation for breast tumor in 2-D sonography. *Ultrasound in Medicine & Biology* 30, 5 (2004), 625-632.
45. Gomez, W., Leija, L., Alvarenga, A.V., Infantosi, A.F.C., and Pereira, W.C.A. Computerized lesion segmentation of breast ultrasound based on marker-controlled watershed transformation. *Medical Physics* 37, 1 (2010), 82-95.
46. Huang, C.S., Wu, C.Y., Chu, J.S., Lin, J.H., Hsu, S.M., and Chang, K.J. Microcalcifications of non-palpable breast lesions detected by ultrasonography: correlation with mammography and histopathology. *Ultrasound in Obstetrics and Gynecology* 13, 6 (1999), 431-436.
47. Chen, C.-M., Chou, Y.-H., Chen, C.S.K., Cheng, J.-Z., Ou, Y.-F., Yeh, F.-C., and Chen, K.-W. Cell-competition algorithm: A new segmentation algorithm for multiple objects with irregular boundaries in ultrasound images. *Ultrasound in Medicine & Biology* 31, 12 (2005), 1647-1664.
48. Cheng, J.-Z., Chou, Y.-H., Huang, C.-S., Chang, Y.-C., Tiu, C.-M., Yeh, F.-C., Chen, K.-W., Tsou, C.-H., and Chen, C.-M. ACCOMP: Augmented cell competition algorithm for breast lesion demarcation in sonography. *Medical Physics* 37, 12 (2010), 6240-6252.

49. Cheng, J.-Z., Chen, C.-M., Chou, Y.-H., Chen, C.S.K., Tiu, C.-M., and Chen, K.-W. Cell-based two-region competition algorithm with a map framework for boundary delineation of a series of 2D ultrasound smages. *Ultrasound in Medicine & Biology* 33, 10 (2007), 1640-1650.
50. Yu, Y. and Acton, S.T. Speckle reducing anisotropic diffusion. *IEEE Trans. on Image Processing* 11, 11 (2002), 1260-1270.
51. Poonguzhali, S. and Ravindran, G. A complete automatic region growing method for segmentation of masses on ultrasound images. In *International Conference on Biomedical and Pharmaceutical Engineering*, 2006, 88-92.
52. Jung, I.-S., Thapa, D., and Wang, G.-N. Automatic segmentation and diagnosis of breast lesions using morphology method based on ultrasound. In *2nd International Conference on Fuzzy Systems and Knowledge Discovery*, L. Wang and Y. Jin, Eds. 2005, Springer, 1079-1088.
53. Shan, J., Cheng, H.D., and Wang, Y. A novel automatic seed point selection algorithm for breast ultrasound images. In *19th International Conference on Pattern Recognition*, 2008, 1-4.
54. Abd-Elmoniem, K.Z., Youssef, A.B.M., and Kadah, Y.M. Real-time speckle reduction and coherence enhancement in ultrasound imaging via nonlinear anisotropic diffusion. *IEEE Trans. on Biomedical Engineering* 49, 9 (2002), 997-1014.
55. Loizou, C.P., Pattichis, C.S., Christodoulou, C.I., Istepanian, R.S.H., Pantziaris, M., and Nicolaides, A. Comparative evaluation of despeckle filtering in

- ultrasound imaging of the carotid artery. *IEEE Trans. on Ultrasonics, Ferroelectrics and Frequency Control* 52, 10 (2005), 1653-1669.
56. Burckhardt, C.B. Speckle in ultrasound B-mode scans. *IEEE Trans. on Sonics and Ultrasonics* 25, 1 (1978), 1-6.
 57. Wagner, R.F., Smith, S.W., Sandrik, J.M., and Lopez, H. Statistics of speckle in ultrasound B-scans. *IEEE Trans. on Sonics and Ultrasonics* 30, 3 (1983), 156-163.
 58. Guo, Y., Cheng, H.D., Tian, J., and Zhang, Y. A novel approach to speckle reduction in ultrasound imaging. *Ultrasound in Medicine & Biology* 35, 4 (2009), 628-640.
 59. Sattar, F., Floreby, L., Salomonsson, G., and Lovstrom, B. Image enhancement based on a nonlinear multiscale method. *IEEE Trans. on Image Processing* 6, 6 (1997), 888-895.
 60. Gupta, S., Chauhan, R., and Sexana, S. Wavelet-based statistical approach for speckle reduction in medical ultrasound images. *Medical and Biological Engineering and Computing* 42, 2 (2004), 189-192.
 61. Kovese, P. Phase congruency: A low-level image invariant. *Psychological Research* 64, 2 (2000), 136-148.
 62. Mulet-Parada, M. and Noble, J.A. 2D+T acoustic boundary detection in echocardiography. *Medical Image Analysis* 4, 1 (2000), 21-30.

63. Kovesi, P.D. *MATLAB and Octave Functions for Computer Vision and Image Processing*. Centre for Exploration Targeting School of Earth and Environment. University of Western Australia, 2009, <http://www.csse.uwa.edu.au/~pk/research/matlabfns/>.
64. Dunn, J.C. A fuzzy relative of the ISODATA process and its use in detecting compact well-separated clusters. *J. Cybernetics* 3, 3 (1973), 32-57.
65. Bezdek, J. *Pattern Recognition with Fuzzy Objective Function Algorithms*. Springer, 1981.
66. Smarandache, F. *A Unifying Field in Logics: Neutrosophic Logic. Neutrosophy, Neutrosophic Set, Neutrosophic Probability*, 3rd ed. American Research Press, 2003.
67. Cheng, H.D. and Guo, Y. A new neutrosophic approach to image thresholding. *New Mathematics and Natural Computation* 4 (2008), 291–308.
68. Smarandache, F. *Neutrosophy: Neutrosophic Probability, Set, and Logic: Analytic Synthesis and Synthetic Analysis*. American Research Press, 1998.
69. Zadeh, L.A. Fuzzy sets. *Information and Control* 8, 3 (1965), 338-353.
70. Zhang, M. *Novel Approaches to Image Segmentation Based on Neutrosophic Logic*. Doctoral Dissertation, Utah State University, 2010.
71. Udupa, J.K., LaBlanc, V.R., Schmidt, H., Imielinska, C., Saha, P.K., Grevera, G.J., Zhuge, Y., Currie, L.M., Molholt, P., and Jin, Y. Methodology for evaluating image-segmentation algorithms. In *Proceedings of SPIE: Medical Imaging*, 2002, 266-277.

CURRICULUM VITAE

Juan Shan
(2011)

EDUCATION

Ph.D. Computer Science May 2011(expected)
 Utah State University (USU), Logan, UT GPA: 3.9
 Dissertation: “*Automatic Lesion Segmentation for Breast Ultrasound Images*”
 Advisor: Heng-Da Cheng

B.S. Computer Science July 2004
 Harbin Institute of Technology (HIT), Harbin, China
 Thesis: “*Protein Family 3D Structure Prediction*”
 GPA ranked top 10 among 400 graduates

RESEARCH INTERESTS

- Image Processing
- Machine Learning
- Computer-aided Diagnosis (CAD)
- Bioinformatics

RESEARCH EXPERIENCE

Graduate Student/Research Assistant June 2005-present

Dr. Cheng’s CVPRIP Research Group, Department of Computer Science, USU

- Main writer and leader of the group to write a survey paper on computer-aided diagnosis systems for breast cancer using ultrasound images. This survey paper was published on *Pattern Recognition* and ranked as #4 on ScienceDirect TOP25 Hottest Articles July-September 2009.
<http://top25.sciencedirect.com/subject/computer-science/7/journal/pattern-recognition/00313203/archive/23/>
- Main writer of several NIH, NSF and DOD grants proposals. Some submitted grant proposals are under review, such as NIH R03 PAR-10-168, NIH R15 PA-10-070, NSF PD 10-7236 (Biophotonics), NSF IIS 10-571 (Information and Intelligent Systems).
- Designed and developed
 - A novel and automatic segmentation algorithm for breast ultrasound images, using neutrosophy solving the fuzzy problems. Comparison with other methods on the same dataset demonstrated the superiority of the proposed method.
 - A completely automatic segmentation algorithm, using multiple domain features. A new phase feature PMO (phase in max orientation) and a distance feature are proposed and proved effective for lesion segmentation.

RESEARCH EXPERIENCE, continued

- An automatic and efficient ROI (region of interest) generation method for breast ultrasound images using region growing.
 - A novel and robust seed point selection algorithm utilizing both texture and spatial features of breast ultrasound images.
 - Participated in the development of
 - A Hidden Markov Model to detect moving vehicles and remove shadows.
 - A pavement detection system for high way maintenance and rehabilitation.
- Dr. Yan's Bioinformatics Research Group, Department of Computer Science, USU
- Designed and developed:
 - A system to analyze the protein-DNA interaction using structure and physicochemical features of proteins, using support vector machine and decision tree, respectively. According to the study, four features were finally selected to be good features which can predict the specificity of amino acid-base contacts.
 - A support vector machine based method to discriminate disease-related non-Synonymous Single Nucleotide Polymorphisms (nsSNPs). Experiment results showed the superiority of the proposed method using the most popular datasets, including Bao and Cui's dataset 2005 and Ye's dataset 2007.

Research Experience for Undergraduates (REU) Site Program in Computer Vision and Image Processing of National Science Foundation, USU

- As a research assistant, I was in charge of four undergraduate students for their research work on REU program. I was responsible for discussing research ideas with them, grading the homework, helping them implement the algorithm and writing papers for research result. One paper was published on top-tier international conference based on my research work on REU.

Undergraduate Research Assistant

September 2003 – July 2004

VILAB, Department of Computer Science, HIT, Harbin, China

- Developed a system to predict protein family using protein 3D structures. Bachelor thesis was based on this work.

TEACHING EXPERIENCE

Instructor, C++ Programming, lab class, 3 sections (CS1710) Fall 2006 & Spring 2008
Department of Computer Science, USU

Coordinated and supervised 3 sections of the lab classes of C++ programming.

Teaching Assistant

Fall 2004 - present

Department of Computer Science, USU

Collaborated on class development and group discussion, met with students upon request, and graded all assignments and programming projects for:

- Evolutionary Computation (CS6655) Spring 2010
- Parallel Programming (CS5500) Spring 2010

TEACHING EXPERIENCE, continued

- Compiler Design (CS5300) Fall 2009 & Fall 2010
- JAVA/Internet Programming (CS3410) Spring 2008
- Advanced Bioinformatics (CS6670) Fall 2008
- Web Development (CS5890) Summer 2007
- Computer Vision, Pattern Recognition and Image Processing (CS5650) Fall 2007
- Introduction to Computer Science-CS 2 (CS1720) Spring 2006
- Algorithms and Data Structure (CS2420) Spring 2005 & Fall 2009
- Software Engineering (CS2450) Fall 2004 & Fall 2008

USU International Teaching Assistant Workshop Summer 2005

Prepared syllabus, lecture slides, and gave sample lectures on a chosen course.

Got TA Certificate.

PUBLICATIONS

Work under review/revision

1. **J. Shan**, H. D. Cheng and Y. X. Wang, “Completely Automated Segmentation Approach for Breast Ultrasound Images Using Multiple-Domain Features”, *submitted to Ultrasound in Medicine and Biology*.
2. **J. Shan**, H. D. Cheng and Y. X. Wang, “A Novel Segmentation Method for Breast Ultrasound Images Based on Neutrosophic L-Means Clustering”, *submitted to Pattern Recognition*.

Journals

1. H. D. Cheng, **J. Shan**, W. Ju, Y. Guo and L. Zhang, “Automated Breast Cancer Detection and Classification Using Ultrasound Images: A Survey”, *Pattern Recognition*, Vol. 43, Issue 1, pp. 299-317, 2010. (5-Year Impact Factor: 3.453)
***Ranked #4 on ScienceDirect TOP25 Hottest Articles July-September 2009**
2. W. Ju, **J. Shan**, C. Yan and H. D. Cheng, “Discrimination of Disease-Related non-Synonymous Single Nucleotide Polymorphism using Multi-Scale RBF Kernel Fuzzy Support Vector Machine”, *Pattern Recognition Letters*, Vol. 30, Issue 4, pp. 391-396, March 2009.

Conferences

1. **J. Shan**, Y. X. Wang and H. D. Cheng, “Completely Automatic Segmentation for Breast Ultrasound Using Multiple-Domain Features”, *Int. Conf. on Image Processing (ICIP2010)*, Hong Kong, China, September 26-29, 2010. (Oral presentation, acceptance rate 47%)
2. **J. Shan**, H. D. Cheng and Y.X. Wang, “A novel automatic seed point selection algorithm for breast ultrasound images”, *Proc. of the 19th International Conference on Pattern Recognition (ICPR 2008)*, Florida, USA, Dec 8-11, 2008. (Acceptance rate 38%)
3. **J. Shan**, H. D. Cheng and Y.X. Wang, “A completely automatic segmentation method for breast ultrasound images using region growing”, *11th Joint Conference on Information Science*, Shenzhen, China, Dec 15-20, 2008.

PUBLICATIONS, continued

4. Y.X. Wang, H. D. Cheng and **J. Shan**, “Detecting shadows of moving vehicles based on HMM”, *Proc. of the 19th International Conference on Pattern Recognition (ICPR 2008)*, Florida, USA, Dec 8-11, 2008. (Acceptance rate 38%)
5. **J. Shan**, Y. Wang and C. Yan, “Toward the recognition code of protein-DNA recognition”, *Proc. of IEEE 7th International Symposium on BioInformatics and BioEngineering*, pp. 1290 – 1293, 2007. (Acceptance rate 13%)
6. **J. Shan**, W. Ju, C. Yan and H. D. Cheng, “Discrimination of Disease-Related Non-Synonymous Single Nucleotide Polymorphism Using Fuzzy Support Vector Machine”, *10th Joint Conference on Information Science*, 2007. (Oral presentation)
7. W. Ju, **J. Shan**, C. Yan and H. D. Cheng, “Discrimination of Outer Membrane Proteins using Fuzzy Support Vector Machines”, *10th Joint Conference on Information Science*, 2007.
8. M. Wacht, **J. Shan**, and X. J. Qi, “A Short-Term and Long-Term Learning Approach for Content-Based Image Retrieval”, *Int. Conf. on Acoustics, Speech, and Signal Processing*, pp. 389-392, Toulouse, France, May 14-19, 2006. (Acceptance rate $1465/3045=48\%$)

PRESENTATIONS

1. **J. Shan**, “Completely Automatic Segmentation for Breast Ultrasound Using Multiple-Domain Features”, *Int. Conf. on Image Processing (ICIP2010)*, Hong Kong, China, September, 2010.
2. **J. Shan**, “Completely Automatic Segmentation for Breast Ultrasound”, *Intermountain Graduate Research Symposium 2010*, Logan, UT, March, 2010.
3. **J. Shan**, “Discrimination of Disease-Related Non-Synonymous Single Nucleotide Polymorphism Using Fuzzy Support Vector Machine”, *10th Joint Conference on Information Science*, Salt Lake City, UT, July, 2007.

AWARDS AND HONORS

- **Dissertation Fellowship** (\$5000.00), USU, Logan, UT, 2010
- **Enhancement Awards** (\$4000.00), Graduate Student Senate, USU, Logan, UT, 2010
- Listed on **Honor Roll of Graduate School**, USU, Logan, UT, 2006
- **Best International TA** on Teaching Assistant Workshop, USU, Logan, UT, 2005
- **Outstanding Graduation** of Heilongjiang Province, China, 2004
- **People Fellowship, First Prize**, Harbin Institute of Technology, China, 2000-2004
- **Guang-Hua Fellowship**, Harbin Institute of Technology, China, 2003
- **Excellent Student Activity Leader**, Harbin Institute of Technology, China, 2002-2004

GRANTS

- **Travel Grant** (\$1100.00) to attend *Int. Conf. on Image Processing (ICIP2010)* at Hong Kong, IEEE Signal Processing Society, 2010.
- **Research& Projects Grant** (\$519.00), Graduate Student Senate, USU, 2010.
- **Travel Grant** (\$500.00), Center for Women and Gender, USU, 2010.
- **Travel Award** (\$300.00), Graduate Student Senate, USU, 2010.

PROGRAMMING SKILLS

Proficient: Matlab, C/C++
 Familiar: Java, R, C#, SQL
 Platform: Windows and Linux systems

PROFESSIONAL MEMBERSHIPS

IEEE Signal Processing Society
 IEEE Women in Engineering

AD HOC REVIEWER

International Conference on Computer Vision, Pattern Recognition & Image Processing 2007
 International Journal of Pattern Recognition and Artificial Intelligence
 International Journal of Image and Graphics
 Digital Signal Processing
 Medical Physics

SERVICE AND ACTIVITIES

- Performer (dancer) at the International Culture Banquet for Chinese New Year, USU, Logan, UT, 2007
- Officer of Student Union of Computer Science Department, Harbin Institute of Technology, China, 2002-2004

LANGUAGES

English (fluent), Chinese (native)